Supporting Information

Face-on Oriented Self-Assembled Molecules with Enhanced π-π Stacking for Highly Efficient Inverted Perovskite Solar Cells on Rough FTO Substrate

*Jiajun Du[1], Jinling Chen[1], Beilin Ouyang[1], Anxin Sun[1], Congcong Tian[1], Rongshan Zhuang[1], Chen Chen[2], Shuo Liu[2], Qianwen Chen[1], Ziyi Li[1], Xiling Wu[1], Jingyu Cai[1], Yuyang Zhao[1], Ran Li[1], Teng Xue[1], Tiantian Cen[1], Kaibo Zhao[1], Chun-Chao Chen[1]**

[1]School of Materials Science and Engineering

Shanghai Jiao Tong University

Shanghai 200240, P. R. China

E-mail: c3chen@sjtu.edu.cn

[2]Future Energy Research Institute of Shanghai,

Contemporary Amperex Technology Co. Limited (CATL),

Shanghai, 200240, P. R. China

Keywords: Inverted perovskite solar cells, self-assembled molecule (SAM), buried interface, voltage loss

Experimental Section

1. Materials

All chemicals were used as received without further purification. Formamidine iodide (FAI, >99.5%) was gained from Greatcell Solar Materials Pty Ltd. [4-(3,6-Dimethoxy9H-carbazol-9-yl) butyl] phosphonic acid (MeO-4PACz, 99%), Cesium iodide (CsI, >99.99%), methylammonium bromide (MABr,>99.5%), Lead(II) bromide ($PbBr_2$, >99.99%), formamidine chloride, methylammonium chlorine (MACl, >99.5%), Bathocuproine (BCP), piperazinium diiodide (PDI), (4-(9'-phenyl-9H,9'H-[3,3'-bicarbazol]-9-yl) butyl) phosphonic acid (4PABCz), [4- (9H-carbazol-9-yl) butyl] phosphonic acid(4PACz) and (4-(3-phenyl-9H-carbazol-9-yl) butyl) phosphonic acid (P-4PACz) are purchased from Xi'an Yuri Solar Co., Ltd. [6,6]-Phenyl-C61-butyric acid methyl ester (PCBM) is gained from Lumtec, Taiwan. Lead (II) iodide (PbI_2, >99.99%) is gained from Xi'an E-Light New Material Company Limited. N, N dimethylformamide (DMF, 99.8%), dimethyl sulfoxide (DMSO, 99.8%), isopropanol (IPA, 99.5%), chlorobenzene (CB), 9-Phenyl-9H,9'H-[3,3']bicarbazolyl(PB-Cz), 3-phenyl-9H-carbazole (P-Cz), methanol (MeOH, 99.9%) and polymethyl methacrylate (PMMA) were obtained from Sigma Aldrich Chemical Company Limited. Tetrahydrofuran (THF) was gained from Shanghai Aladdin Biochemical Technology Company

Limited. The FTO substrate (model number: HM-FTO-22), purchased from Beijing Huamin New Materials Technology Co., Ltd, possesses a square resistance of 8 ohms, and a thickness of 2.2 mm. An anti-reflective film (BA4076, Japan) was also placed on the back of the FTO glass.

2. Perovskite film fabrication

First, FAI, MABr, PbI_2, $PbBr_2$, CsI were fully dissolved in mixed solvents of DMF and DMSO (4:1, v/v) according to the stoichiometric formula of 1.5M $Cs_{0.05}(FA_{0.98}MA_{0.02})_{0.95}Pb(I_{0.98}Br_{0.02})_3$ in anhydrous DMF: DMSO =4:1 (v:v) with 15 mol% MACl. Then, the solution was stirred at room temperature until dissolved. The precursor solution was filtered through a 0.22 μm polytetrafluoroethylene filter before use. A portion of 60 μl of perovskite solution was deposited on the substrate and spun cast at 2,000 rpm for 10 s, followed by 5,000 rpm for 40 s. A 200 μl portion of CB as an anti-solvent was dropped onto the substrate during the last 10 s of spinning. Then, quickly transferred the substrates to annealing at 110 ℃ for 20 min.

3. Fabrication of integrated devices

The glass/FTO substrate underwent a cleaning process, which included ultrasonic treatment in sequential baths of anhydrous ethyl alcohol, detergent, deionized water, acetone, and isopropanol. Afterward,

the substrate was dried and then subjected to a 15-minute exposure in a UV-ozone environment to remove organic contaminants. Then, FTO substrates were transferred into the nitrogen-filled glovebox quickly maintaining less than 0.1 ppm of O_2 and H_2O. After cooling down to room temperature, for devices using MeO-4PACz, 4PACz, P-4PACz, and 4PABCz as the HSLs, a solution at a concentration of 1 mmol/L in methanol was spin-coated at 3000 rpm for 30 seconds and annealed at 100 °C for 10 minutes. Perovskite solution was deposited on the SAM-modified substrate as detailed above. Subsequently, a 1 mg/mL PDI solution in IPA was spin-coated on the perovskite layer at 5000 rpm for 30 seconds and annealed at 100 °C for 10 minutes. Then, PCBM (20 mg/mL in CB) was spin-coated at 2000 rpm for 30 s and BCP (saturated solution in IPA) was spin-coated at 5000 rpm for 30 s. Finally, Ag (100 nm) is deposited as back electrode through a mask by thermal evaporation under 9.9×10^{-5} Pa. For the stability assessment, the BCP layer was substituted with a 15 nm SnO_2 atomic layer, which was deposited utilizing an atomic layer deposition (ALD) system (NCE-200R, NanoFrontier, China) with $((CH_3)_2N)_4Sn$ and deionized water as the precursor sources for Sn and O, respectively. Mini-module was prepared in the same way as for the small-area devices. The FTO (5 cm × 5 cm) was cleaned and deposited with 4PABCz layers as described above. The perovskite films were spin-coated onto the substrates and annealed according to the above procedures.

4. Exfoliation of the perovskite films:

Firstly, PMMA (0.4 g PMMA was dissolved in 1 mL CB) was blade coated on the prepared perovskite film, and the coated substrate was annealed at 70 °C for 10 min. After a day at room temperature, perovskite film was peeled off with a tweezer.[1]

5. Characterization

The NMR spectra are recorded on Bruker Avance III (600 MHz). X-ray photoelectron spectroscopy (XPS) was acquired by an AXIS Ultra DLD X-ray photoelectron spectrometer and calibrated against the C 1s peak (284.8 eV). Grazing incidence wide-angle X-ray scattering (GIWAXS) tests are performed at beamline BL14B in the Shanghai Synchrotron Radiation Facility (SSRF) with an X-ray wavelength of 0.124 nm, the GIWAXS patterns are acquired with a grazing incidence angle of 0.3º and an exposure time of 60 s. XRD was tested by Mini Flex 600 X-ray diffractometer (with Cu-Ka radiation as X-ray source) with a scan rate of 15° min^{-1}. The X-ray reflectivity (XRR) measurements of the SAMs and Grazing-incidence X-ray diffraction (GIXRD) were performed using a SmartLab X-ray diffractometer, and GIXRD was under 10-30° scan range with a step size of 0.02°/s. The data for the single crystals of P-Cz and PB-Cz were collected with a D8 VENTURE Single crystals diffractometer with large area photon II detector. The single crystals used for X-ray

diffraction analysis were obtained by slow evaporation in THF. Ultraviolet and visible (UV-vis) spectrophotometry was tested by EV 300 (Thermo Fisher Scientific).PL mapping images were obtained by Raman image scanning electron microscopy (RISE-MAGNA). Steady-state photoluminescence (PL) and time-resolved photoluminescence (TRPL) and PL quantum yield (PLQY) tests were performed using an FLS 1000 photoluminescence spectrometer. SEM images were acquired by field emission scanning electron microscope (JSM-7800F). Kelvin probe force microscopy (KPFM), atomic force microscopy (AFM) and conductive atomic force microscopy (c-AFM) images were observed on the Bruke Bio Fast Scan AFM using taping mode. Ultraviolet photoelectron spectroscopy (UPS) was measured by AXIS Ultra DLD machine under excitation from the He I line (21.22 eV) of a helium discharge lamp. The transient photovoltage (TPV) and transient photocurrent (TPC) curves were measured by a platform for the all-in-one characterization of solar cells (PAIOS) of FLUXim Company. The background light of 1 Sun (100 mW cm−2) was applied. Electrochemical impedance spectroscopy (EIS) spectra and Mott Schottky curve (M-S) are observed on a Chenhua CHI660E electrochemical workstation under dark conditions. The current density-voltage (*J-V*) curves of the device (area: 0.074 cm^2) were obtained under AM1.5G illumination at 100 mW cm-2 (calibrated by a standard VLSI Si reference solar cell (SRC-1000-TC-K-QZ)) using an Abet

Technologies Sun 2000 solar simulator and a Keithley 2400 source meter. External quantum efficiency (EQE) test was performed by the QTEST HIFINITY 5 EQE system (the light intensity was calibrated with standard Si detectors). Space-charge-limited current (SCLC) was measured using a Keithley 2400 system to obtain dark-state *J-V* curves of the FTO/SAM/perovskite/PTAA /Ag structure.

6. Calculation

Geometries optimization and frequency analysis was performed at the B3LYP[2]/6-311G(d,p)[3,4], and a more accurate def2TZVP basis set[5,6] was used for dipole moment calculations. The molecular orbitals and dipole moments were analyzed, and the energy gaps between HOMO and LUMO were obtained. These calculations were based on Density Functional Theory (DFT) with Gaussian 09 package.[7,3,8] The VMD software was used to map the molecular surface electrostatic potential.[9] The electron density level of the van der Waals (vdW) surface was defined as 0.001 e $Bohr^{-3}$, and all molecular size information was calculated by Multiwfn.[10,11]

The calculations about the dimeric system of SAMs were performed using Gaussian at the level of M06-2X/def2-TZVP with DFT-D3 method.[12,13] The interaction region indicator (IRI) analysis was based on the optimal geometry structures of the dimers and analyzed the intermolecular interactions through Multiwfn and gnuplot.[14,15]

The spin-polarized DFT calculations were performed using the Vienna Ab Initio Simulation Package (VASP) code, employing periodic boundary conditions.[16,17] The projector augmented wave (PAW) pseudopotential was used to describe the ion-core electron interaction, while the exchange-correlation energy of valence electrons was described by the Perdew-Burke-Ernzerhof (PBE) functional with a plane-wave cutoff energy of 400 eV.[18,19] Grimme's D3 corrections were also used to describe the dispersion interaction.[12] The energy convergence criteria of structure optimization (including lattice parameters and internal atomic positions) were set to 10^{-5} eV for each self-consistent field (SCF) iteration step, and the maximum force convergence criterion for geometry optimization was set to 0.05 eV/Å. For surface calculations involving both ITO and FAPbI3, a surface/vacuum structure with a vacuum thickness of 15 Å was considered. The adsorption energies (E_{ads}) of SnO_2 or perovskite surface adsorbed by different molecules (4PACz, 4PABCz and P-4PACz) were calculated as E(SAM@SnO2/perovskite) −E(SAM)−E(SnO2/perovskite). The molecular graphics viewer VESTA was used to plot the crystal structures.[20]

Ab initio molecular dynamics (AIMD), were performed with the CP2K package utilizing a mixed Gaussian/plane wave (GPW) basis.[21] The PBE exchange-correlation functional,[22] DFT-D3 dispersion corrections and dipole corrections necessary for periodic boundary conditions along

the perpendicular direction to the surface were included.[12,23] Valence electron wave functions were expanded in a double-ζ Gaussian basis set with polarization functions (DZVP).[24] The energy cutoff for the electron density expansion in the GPW method was 400 Ry. Born-Oppenheimer AIMD simulations were run with an integration time step of 0.5 fs and the system was kept at 300 K using the thermostat of Bussi et al. in a canonical isothermal–isochoric (NVT) ensemble, in which the total number of atoms N, the volume V and the temperature T of the system were held constant.[25,26] All AIMD simulations were performed at Γ point. Being the most stable surface, the SnO_2(110) was chosen as the substrate surface. The initial systems were from geometric optimization structure by DFT and the following 10 ps were used for the production run. To investigate the interactions between the SAMs and the SnO_2 substrate, three configurations were simulated: (1) 4PACz on SnO_2(110); (2) P-4PACz on SnO_2(110); (3) 4PABCz on SnO_2(110). In all the models, an in-plane SnO_2(110) simulation cell of 25.1165 Å × 19.8655 Å with 15 Å of vacuum between the slab repetitions was used. AIMD was also used to estimate the interaction energy of SAMs with the SnO_2(110) surface. OVITO was used to visualize the trajectory of the AIMD simulation.[27]

Classical molecular dynamics simulations were realized with the help of the LAMMPS molecular dynamics simulator.[28] The equations of motion were integrated using the velocity Verlet method, with a 1 fs time step, in

which bond stretching was not constrained for any bonds.[29] To maintain isothermal conditions, the deterministic Nosé–Hoover thermostat with a time constant equal to 0.1 ps was used.[26,30] This ensured that the thermostat was applied to both translational and rotational degrees of freedom. All classical molecular dynamics simulations were realized in the canonical NVT ensemble at T = 373 K comprising a V-shaped SnO_2(110) model system with dimensions 204 Å × 224 Å × 33 Å or a flat SnO_2(110) model system with dimensions 204 Å × 214 Å × 18 Å. Periodic boundary conditions were used in the x and y directions, whereas reflective boundary conditions were used in the z direction.

The systems were equilibrated for 100 ps followed by a 100 ps production simulation, during which sampling took place every 1 ps for the calculation of ensemble averages. To accurately capture the interactions of SnO_2, the thoroughly validated classical force field developed by Bandura et al. was used.[31] For SAMs, containing the phosphonic functional group, the specially designed force field developed by Meltzer et al. based on the generalized Amber force field was used.[32] The van der Waals and electrostatic non-bonded interactions were calculated using a real-space cutoff radius of 12 Å and 12 Å, respectively. The surface coverage calculations identified the surface area covered by the atoms of the SAMs less than 4 Å to the surface in OVITO.

7. Calculation of quasi-Fermi level splitting (QFLS) and $\Delta Voc-imp\ nonrad$

QFLS can be obtained from PLQY by the following formula:[33,34]

$$QFLS = QFLS_{rad} + kBTln(PLQY)$$

$$QFLS_{rad} = kBTln\left(\frac{JG}{J_{0,rad}}\right) + kBTln(PLQY)$$

where $QFLS_{rad}$ is the radiation limit of semiconductor materials, which sets the maximum achievable splitting of the quasi-Fermi level without considering nonradiative radiation recombination. k_B is the Boltzmann constant, J_G is the photogenerated current density, $J_{0,rad}$ is the dark state radiative recombination saturation current density. According to the detailed balance theory, $J_{0,rad}$ can be calculated by the following equations:

$$J_{0,rad} = q\int_0^{\infty} EQE(E)\emptyset_{BB}(E)dE$$

$$\emptyset_{BB}(E) = \frac{2\pi E^2}{h^3c^2}\frac{1}{\exp\left(\frac{E}{k_BT}\right)-1}$$

where q is the elementary charge, EQE is the photovoltaic external quantum efficiency, Φ_{BB} is the black-body radiative spectrum, E is the photo energy, h is the Planck constant, and c is the light speed in vacuum.

V_{oc} nonradiative recombination loss $\Delta V_{oc-imp}^{nonrad}$ can be calculated by the following equation:

$$q\Delta V_{oc-imp}^{nonrad} = QFLS_{rad} - QFLS = -k_BTln(PLQY)$$

8. Stress test using GIXRD

According to Bragg's Law and generalized Hooke's Law,[35] 2θ-sin^{2}φ can be given by:

$$\sigma = -\frac{E}{2(1+v)}\frac{\pi}{180^\circ}cot\theta 0\frac{\partial(2\theta)}{\partial sin2\varphi}$$

where E is the perovskite modulus, v is the Poisson's ratio of the perovskite, and θ_0 is half of the scattering angle $2\theta_0$, which corresponds to a given diffraction peak for stress-free perovskite ($2\theta_0$, 31.73°). It should be noted that 2θ is the scattering angle for the actual perovskite and φ is the angle of diffraction vector N_k with respect to the sample surface normal. For the high diffraction angle and multiplicative factor of the (012) plane, we chose it as the analysis object for GIXRD measurement. By fitting 2θ as function of sin^{2}φ, the stress of perovskite can be calculated. The slope of the fitted line denotes the scale of the residual strain. And the negative slope indicates that the films bear tensile stress, while the positive slope indicates the films bear compressive stress.

9. TRPL

The TRPL decay curves were fitted by the bi-exponential function:

[36]

$$f(t) = A_1\, exp^{(\frac{-t}{\tau_1})} + A_2\, exp^{(\frac{-t}{\tau_2})} + B$$

$$\tau_{ave} = \frac{\sum A_i\tau_i^2}{\sum A_i\tau_i}$$

Here, τ_1 is the fast transient component, τ_2 is the slow component, A_1 and A_2 are constants, and B is the constant for the baseline offset.

10. SCLC

The dark *J-V* curves of electron-only devices can be divided into three parts, i.e., the ohmic region, trap-filling limited region with a sharp increase in current, and trap-free child's region. The trap density (N_t) of perovskite films can be calculated as follows[37]:

$$N_t = \frac{2V_{VFL}\varepsilon_r\varepsilon_0}{qL^2}$$

where ε_r is the relative dielectric constant of perovskite, ε_0 is the vacuum dielectric constant, q is the electric charge, and L is the thickness of perovskite film.

11. FF Loss

The FF loss between Shockley-Queisser (S-Q) limit value of FF and the FF measurement value consists of non-radiative recombination loss and charge transport loss. The FF maximum value (FF_{max}) without charge transport loss can be determined by the following equation:[38,39]

$$FF_{max} = \frac{qV_{oc} - nk_BTln(qV_{oc} + o.72nk_BT) - nk_BTln(nk_BT)}{qV_{oc} + nk_BT}$$

where q is the elementary charge, n is the ideal factor, k_B is Boltzmann constant, T is thermal equilibrium temperature. The ideal factor

(n) can be obtained by measuring the change of open circuit voltage (V_{oc}) with light intensity. The calculation method is as follows:

Here, I is the light intensity and n is the ideality factor used to determine the carrier compound type.[40]

$$\frac{\partial V_{oc}}{\partial(\ln I)} = n\frac{k_B T}{q}$$

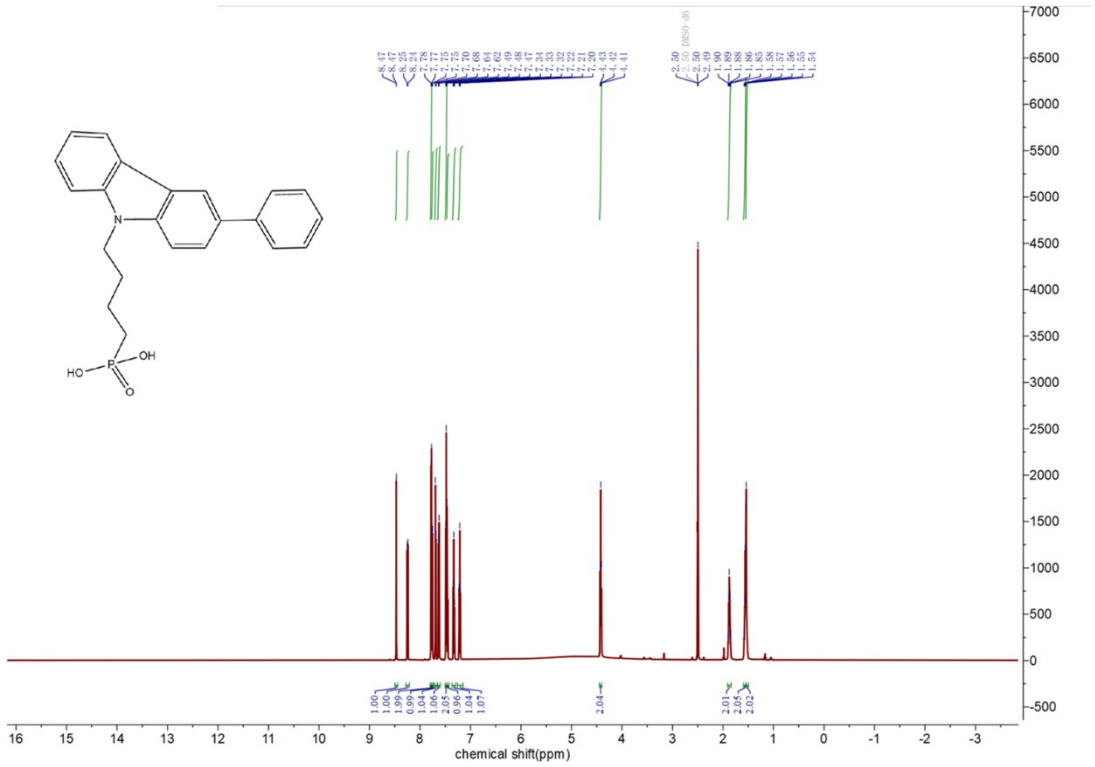

Figure S1. ^{1}H NMR spectrum for P-4PACz in DMSO-d_6.

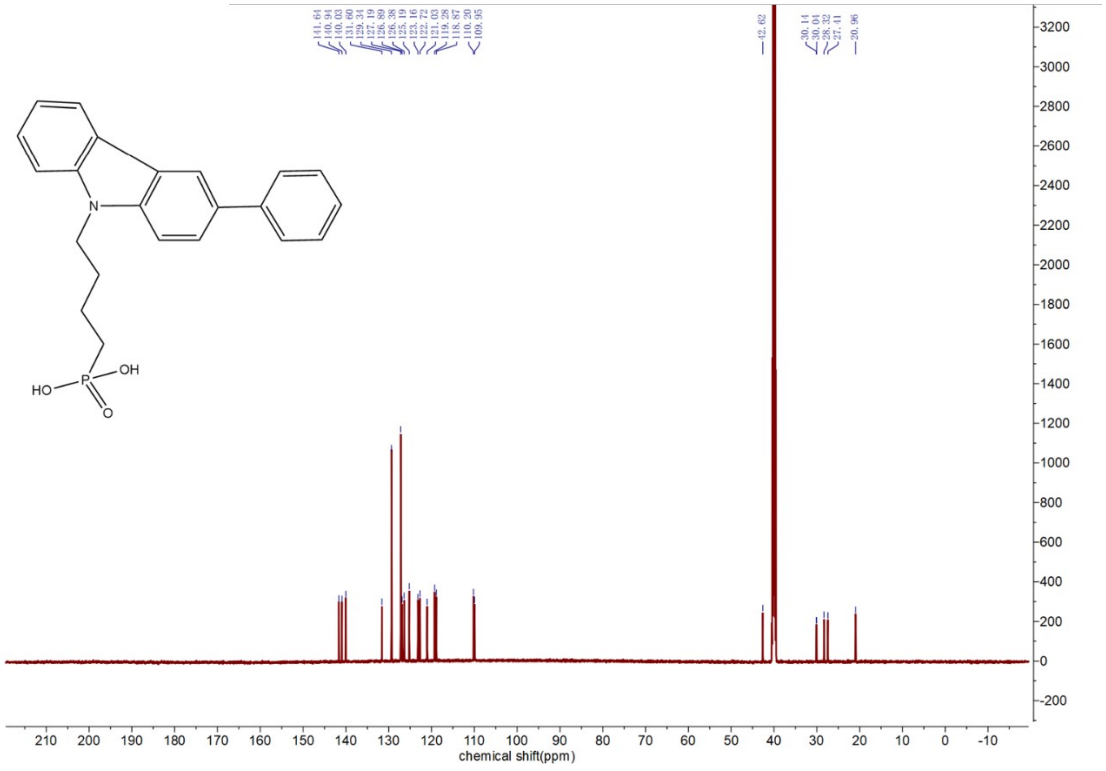

Figure S2. ^{13}C NMR spectrum for P-4PACz in DMSO-d_6.

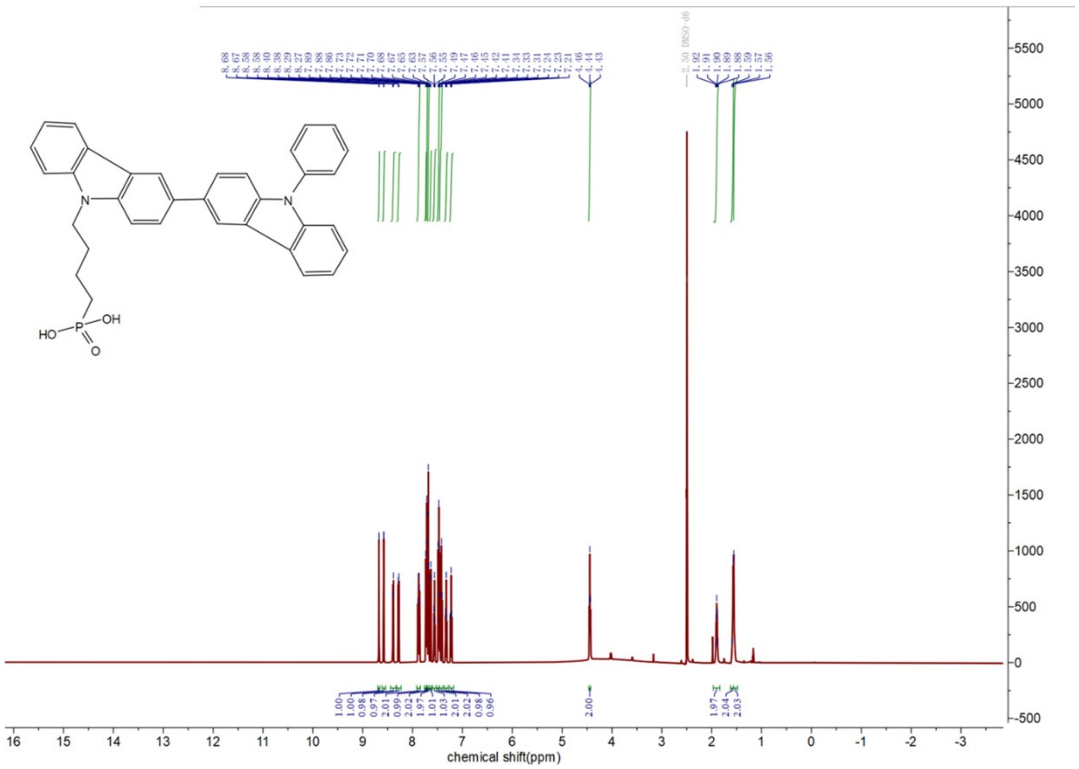

Figure S3. ^{1}H NMR spectrum for 4PABCz in DMSO-d_6.

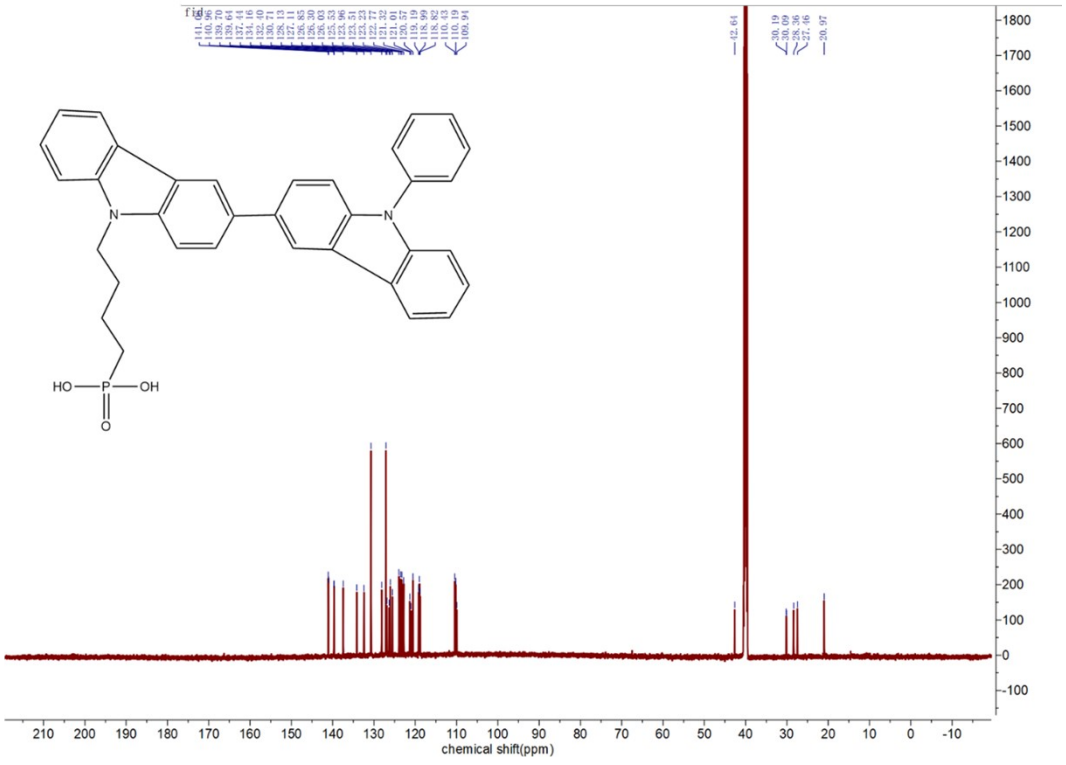

Figure S4. ^{13}C NMR spectrum for 4PABCz in DMSO-d_6.

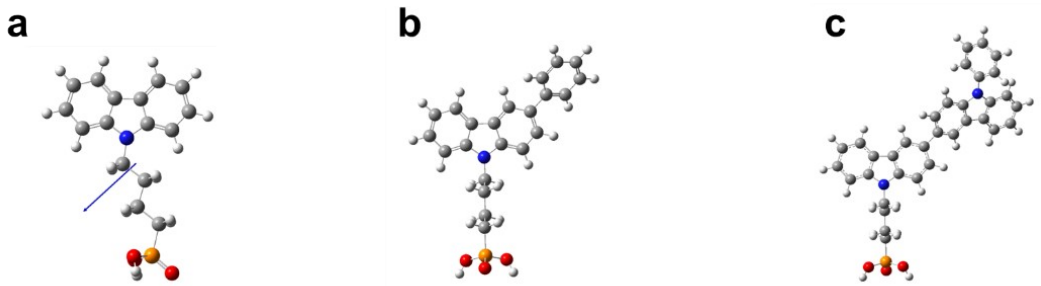

Figure S5. Front views of calculated molecular structures with dipole direction of a) 4PACz, b) P-4PACz and c) 4PABCz.

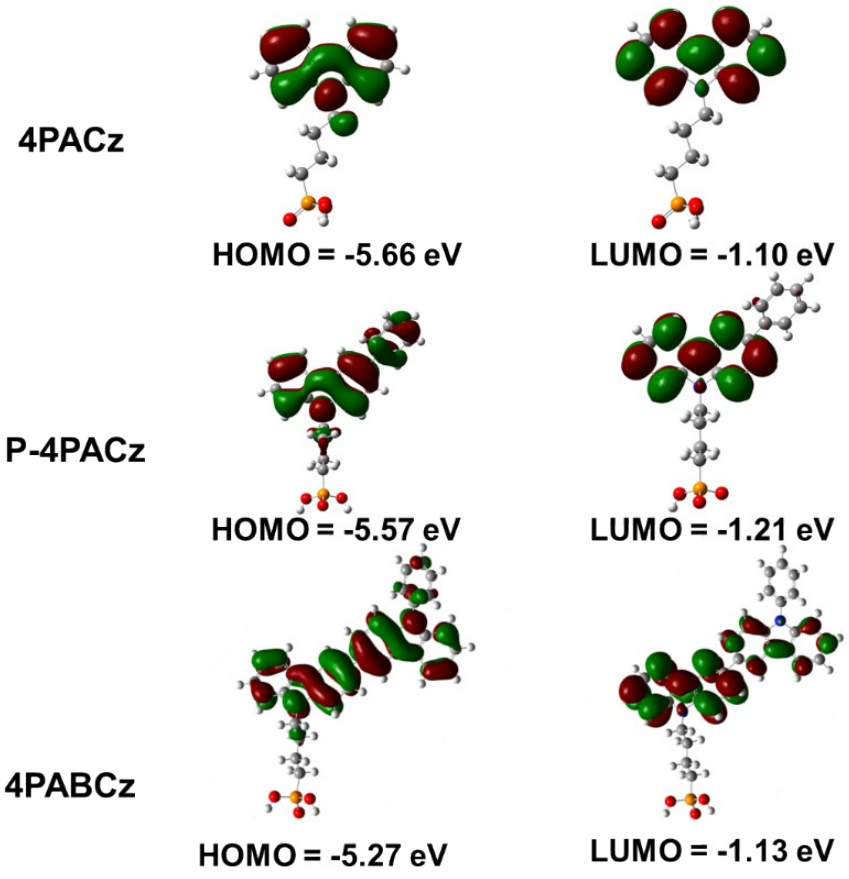

Figure S6. The highest occupied molecular orbital (HOMO) energy levels and the lowest unoccupied molecular orbital (LUMO) energy levels of 4PACz, P-4PACz and 4PABCz.

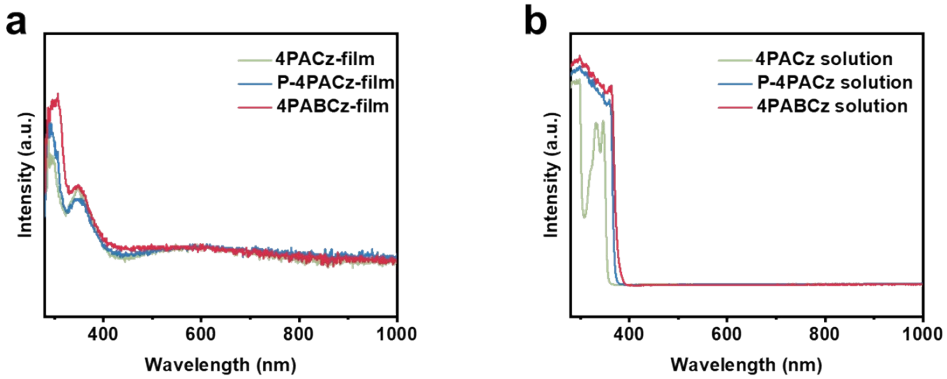

Figure S7. a) UV-vis absorption spectra of 4PACz, P-4PACz and 4PABCz films. b) UV-vis absorption spectra of 4PACz, P-4PACz and4PABCz solutions in THF.

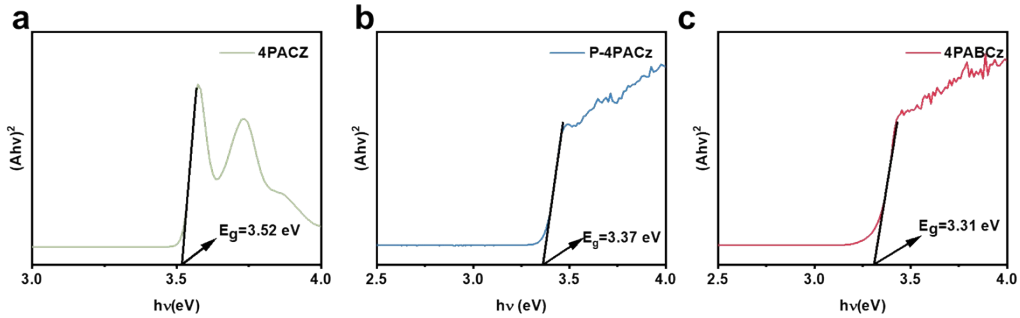

Figure S8. Tauc plots of a) 4PACz, b) P-4PACz and c)4PABCz films obtained from UV-vis absorption spectra in Figure S7 a).

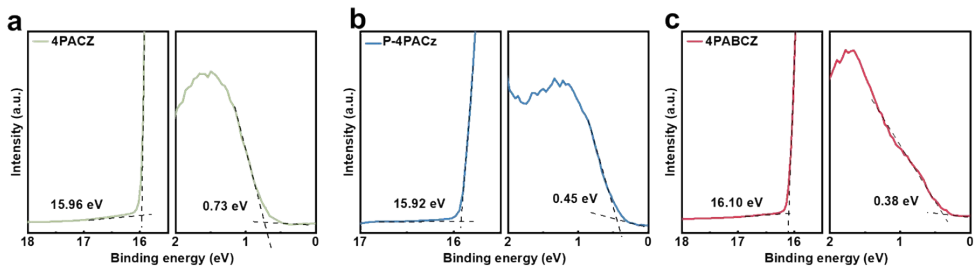

Figure S9. UPS spectra of a) 4PACz-modified FTO, b) P-4PACz-modified FTO and c) 4PABCz-modified FTO.

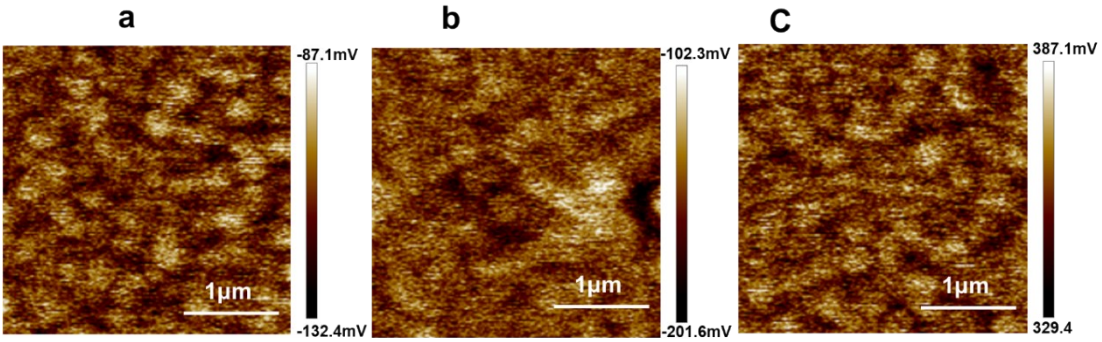

Figure S10. Kelvin probe force microscopy (KPFM) images of a) FTO/4PACz, b) FTO/P-4PACz and c) FTO/4PABCz.

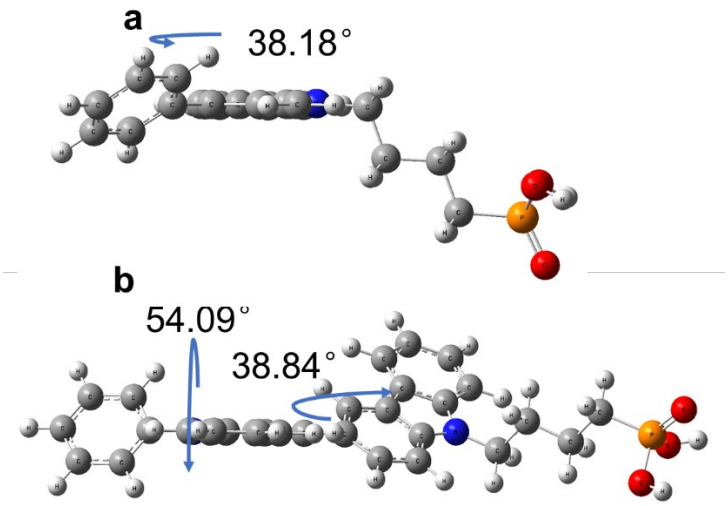

Figure S11. Dihedral angles of a) P-4PACz and b) 4PABCz.

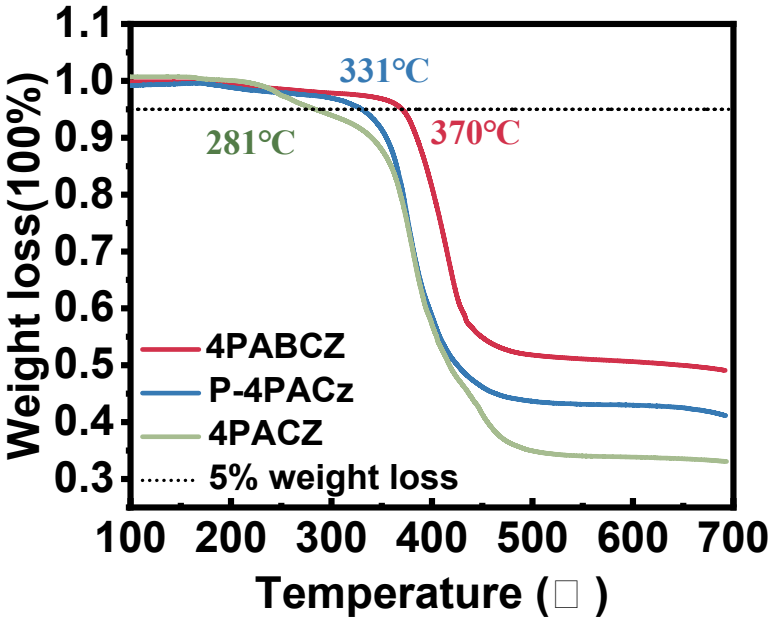

Figure S12. Thermogravimetric analysis (TGA) curves of 4PACz, P-4PACz and 4PABCz; heating rate: 10 °C/min, from RT to 700 °C under nitrogen atmosphere.

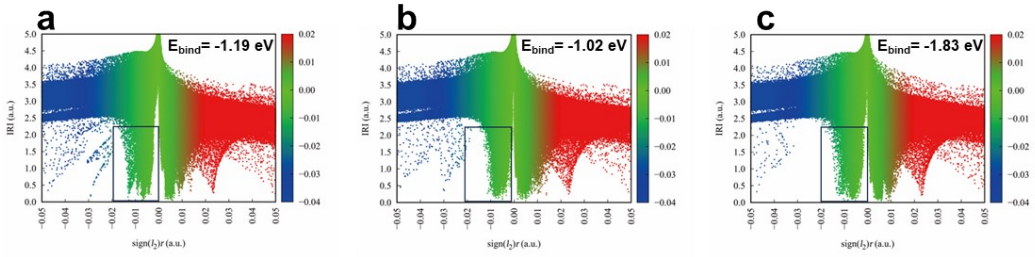

Figure S13. The interaction region indicator (IRI) analysis of a) 4PACz, b) P-4PACz and c) 4PABCz dimer and the binding energy (E_{bind}) were shown.

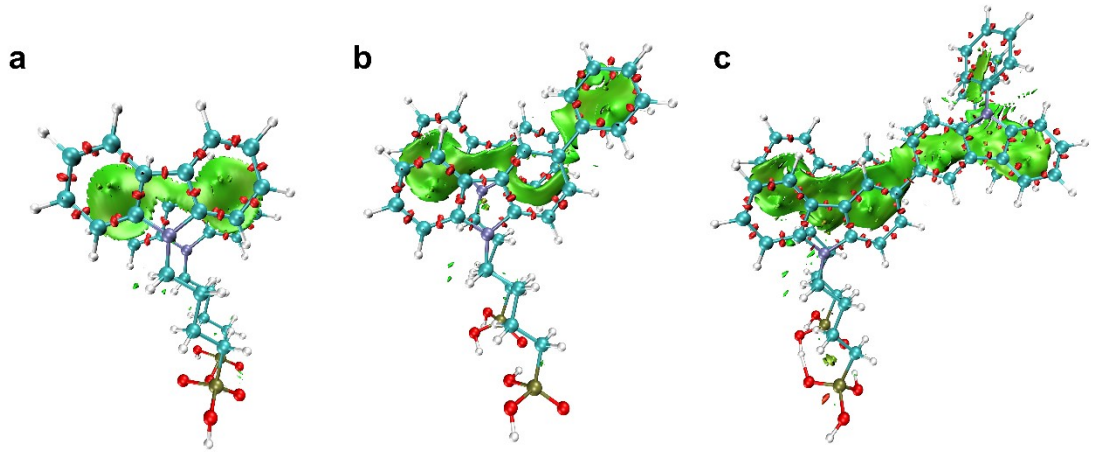

Figure S14. The IRI-π analysis of a) 4PACz, b) P-4PACz and c) 4PABCz dimers (only π-electrons are included in the analysis).

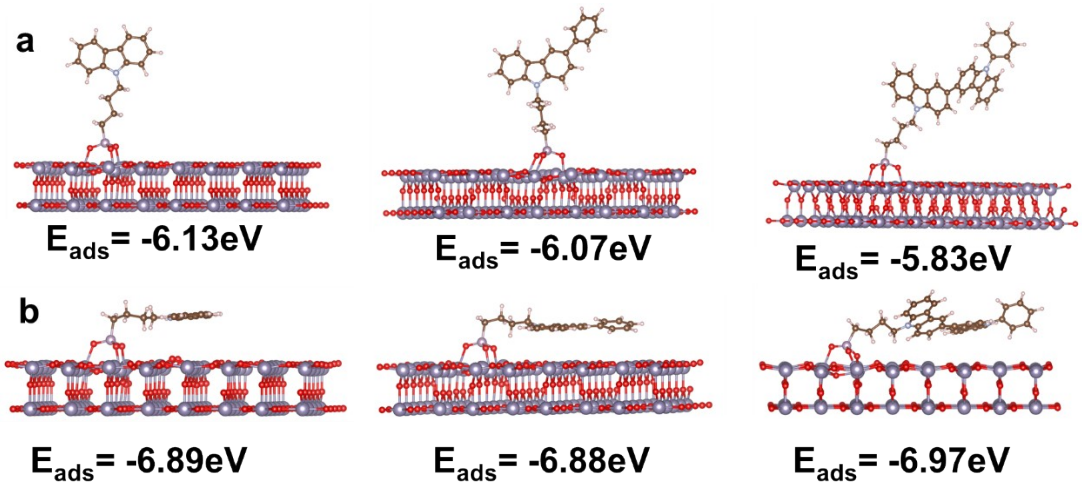

Figure S15. The adsorption energy of 4PACz, P-4PACz and 4PABCz after dehydrogenation reaction with a) perpendicular and b) parallel to the substrate.

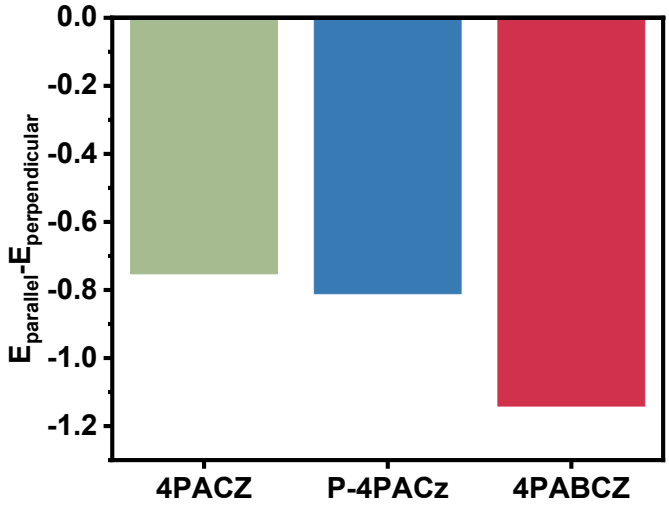

Figure S16. The formation energy difference between parallel and perpendicular ligand-surface orientations ($E_{para} - E_{perp}$) of SAMs after dehydrogenation reaction.

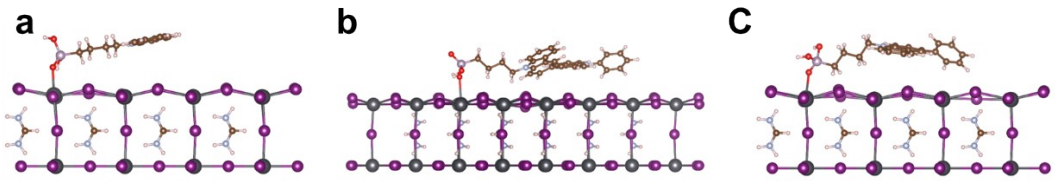

Figure S17. The adsorption structures of a) 4PACz, b) P-4PACz and c) 4PABCz with parallel orientation at the perovskite surface.

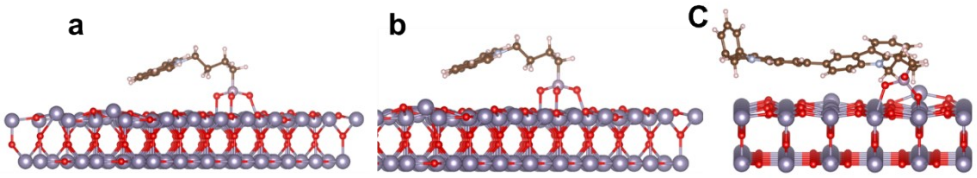

Figure S18. Schematic diagrams of final states in AIMD of a) 4PACz, b) P-4PACz and c) 4PABCz.

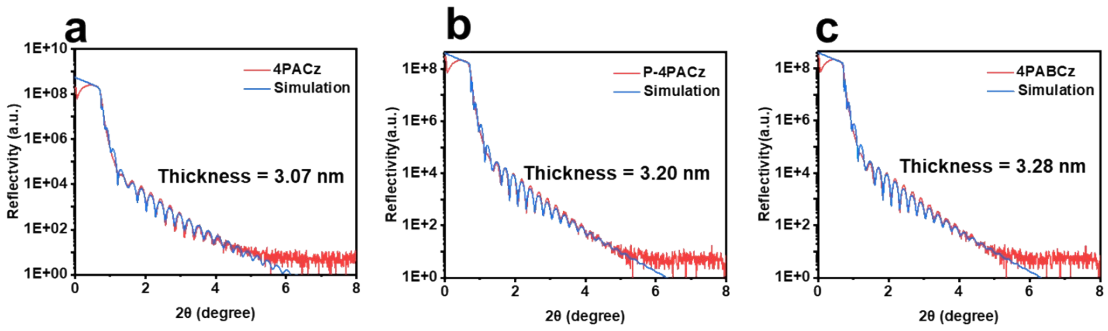

Figure S19. XRR measurements of a) 4PACz, b) P-4PACz and c) 4PABCz.

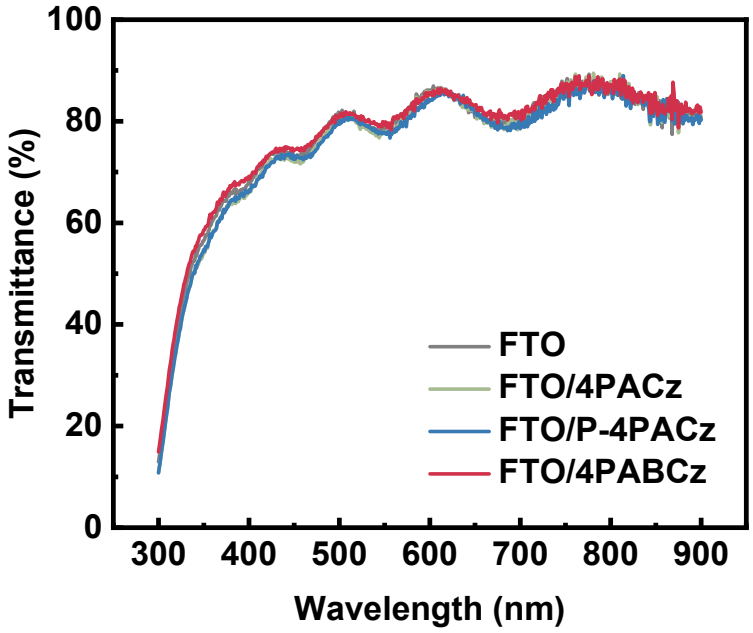

Figure S20. UV-vis transmittance of 4PACz, P-4PACz and 4PABCz films on FTO substrates with bare FTO substrate as control.

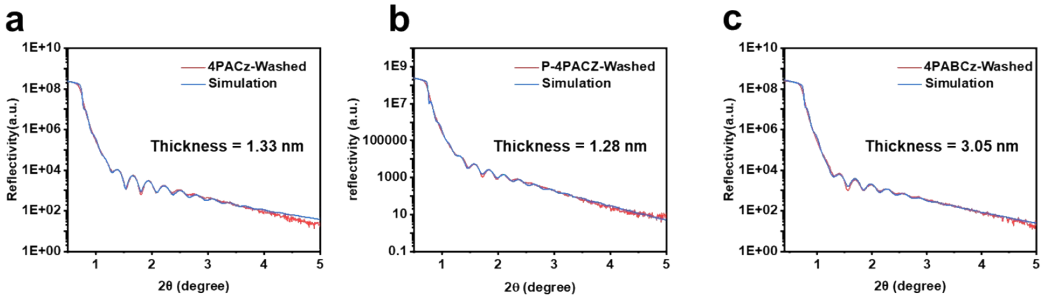

Figure S21. XRR measurements of a) 4PACz, b) P-4PACz and c) 4PABCz films after rinsing with a solution of DMF and DMSO in a ratio of 4:1.

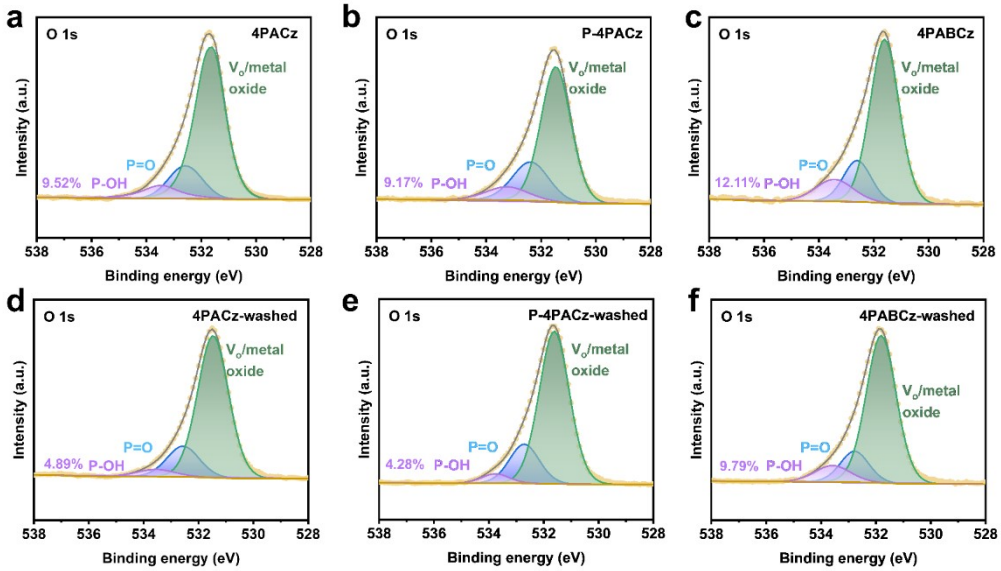

Figure S22. XPS spectra of O 1s on (a,d) 4PACz, (b,e) P-4PACz and (c,f) 4PABC films before and after washing by a polar solvent mixture (DMF: DMSO = 4:1 in volume).

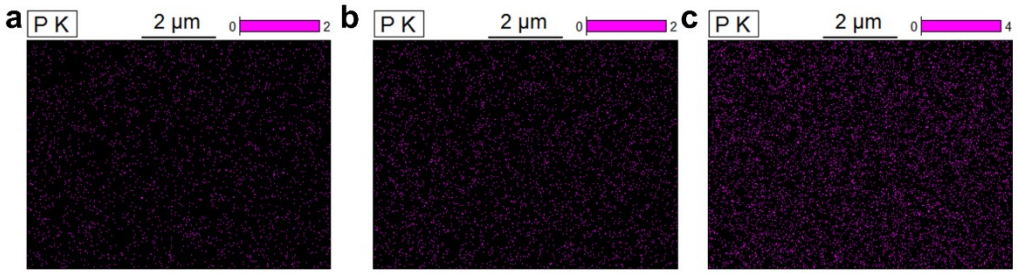

Figure S23. Elemental mapping of P for a)4PACz, b) P-4PACz and c) 4PABCz modified substrate.

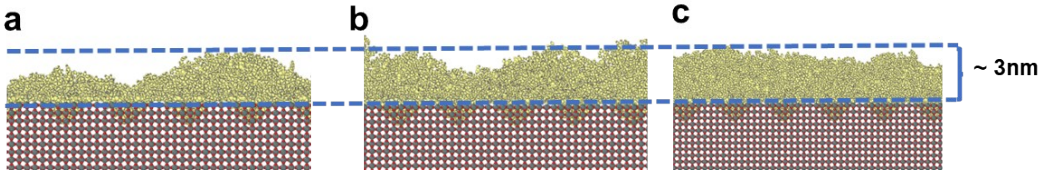

Figure S24. Side views of equilibrated molecular representations of the

heterojunctions with a) 4PACz, b) P-4PACz and c) 4PABCz

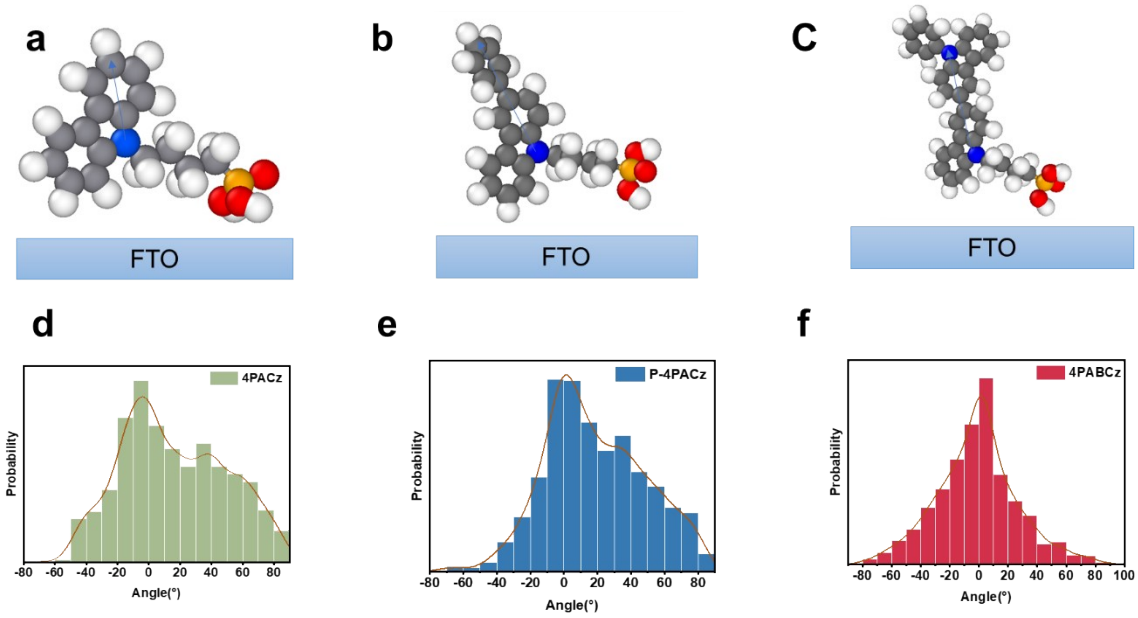

Figure S25. Schematic of the specific vector in a) 4PACz, b) P-4PACz and c) 4PABCz.The angles of vector in conjugate planes of d) 4PACz, e) P-4PACz and f) 4PABCz with respect to SnO_2 surface.

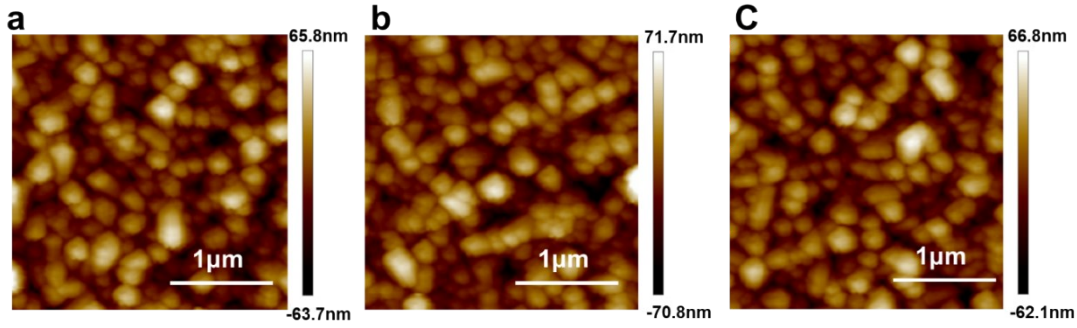

Figure S26. AFM images of a) 4PACz, b) P-4PACz and c) 4PABCz on FTO.

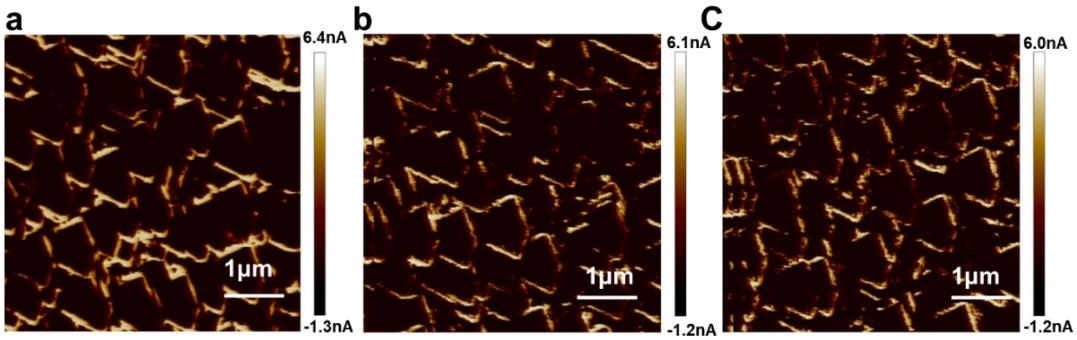

Figure S27. Conductive AFM (c-AFM) images of a) 4PACz, b) P-4PACz and c) 4PABCz on FTO.

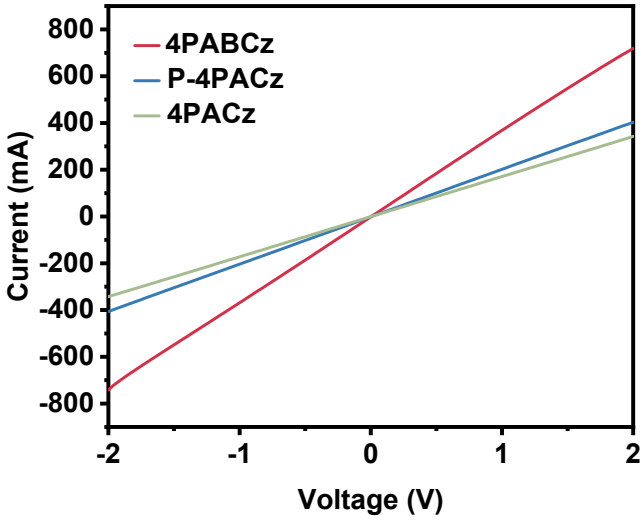

Figure S28. *I–V* curves of the hole-only devices to evaluate the hole transport ability of SAMs. The device configuration was FTO/SAMs/Ag.

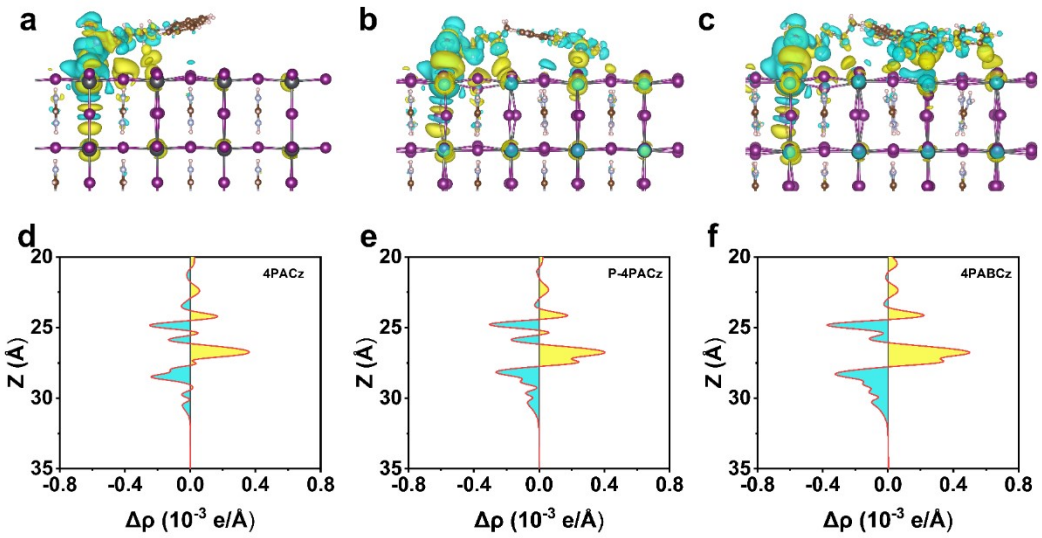

Figure S29. (a-c) Charge density difference plots for perovskite/SAMs interfaces. (d-e) The planar average charge density along the z direction (The yellow region indicates electron accumulation, while the cyan region indicates electron depletion).

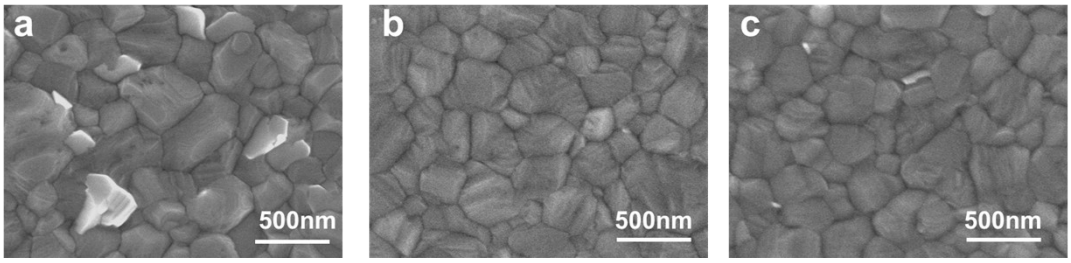

Figure S30. SEM images of perovskite surface modified by a) 4PACz, b) P-4PACz and c) 4PABCz films.

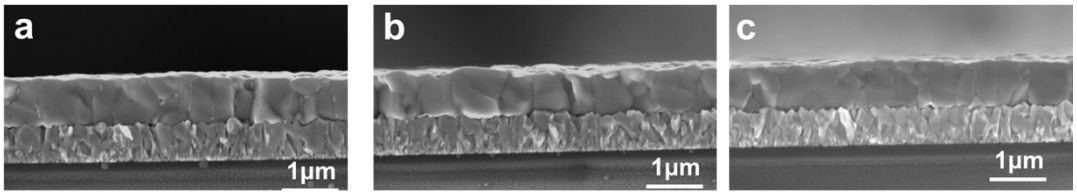

Figure S31. Cross-sectional SEM image of perovskite films based on a)

4PACz, b) P-4PACz and c) 4PABCz films with FTO substrate.

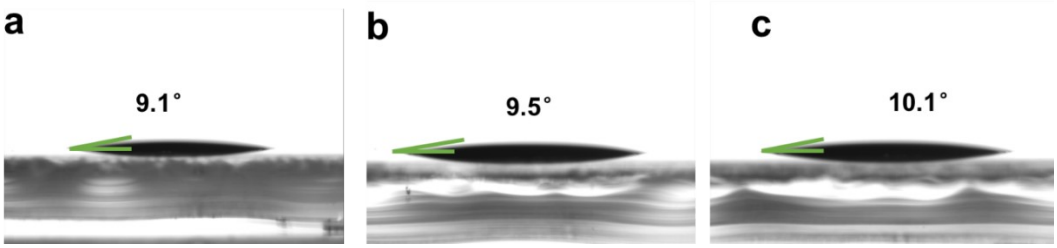

Figure S32. The contact angles of perovskite droplets formed on a) 4PACz, b) P-4PACz and c) 4PABCz films with FTO substrate.

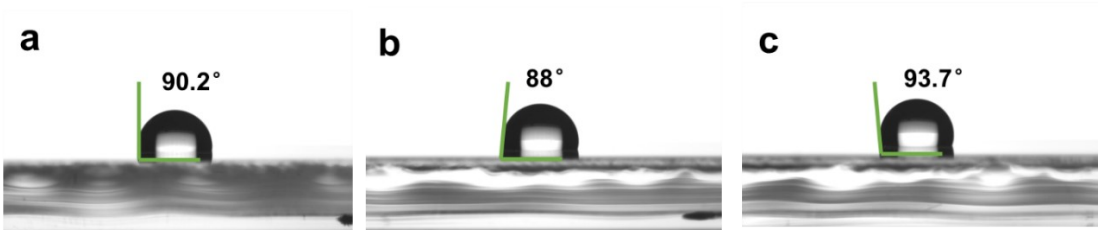

Figure S33. The contact angles of water droplets formed on a) 4PACz, b) P-4PACz and c) 4PABCz films with FTO substrate.

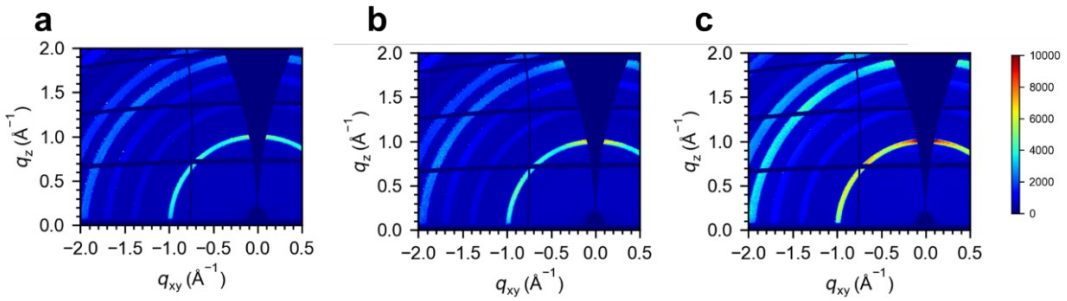

Figure S34. GIWAXS patterns for perovskite films deposited on a) 4PACz, b) P-4PACz and c) 4PABCz films with Si substrate.

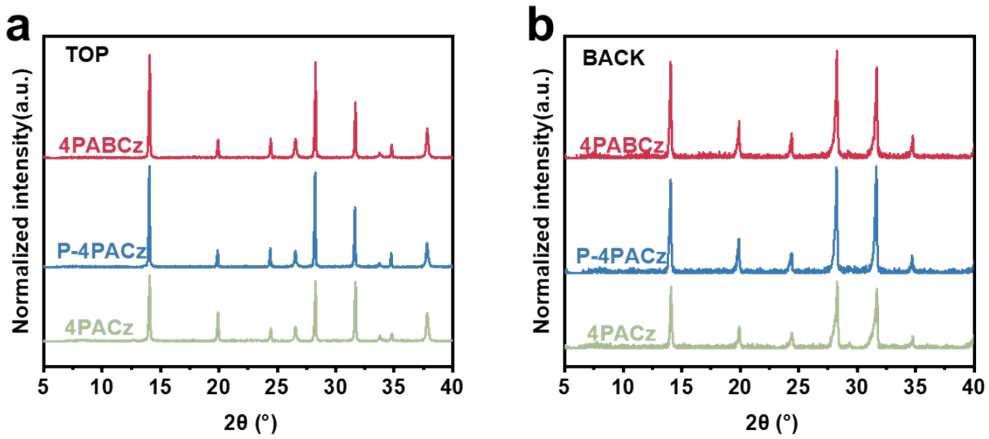

Figure S35. The XRD patterns of 4PACz, P-4PACz and 4PABCz perovskite films on a) the top surface and b) the buried surface.

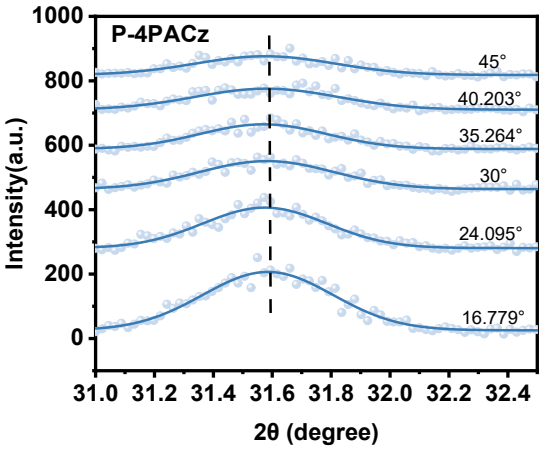

Figure S36. GIXRD patterns measured at different ψ angles from 16° to 45° for perovskite films on P-4PACz/FTO.

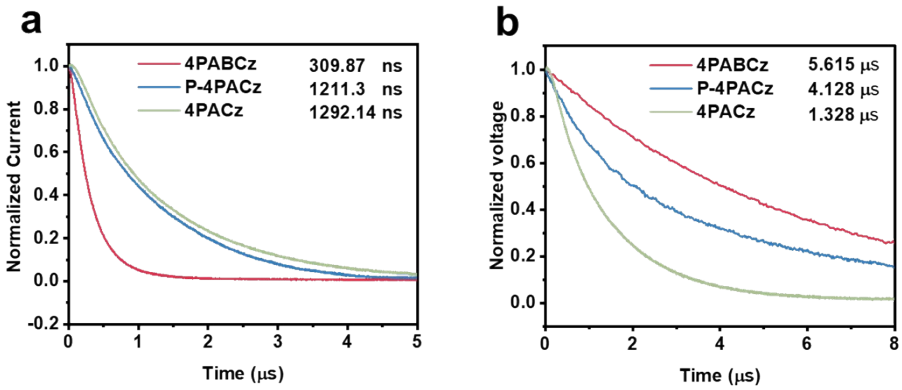

Figure S37. (a) TPC and (b) TPV decay curves of PSCs based on 4PACz, P-4PACz and 4PABCz films respectively.

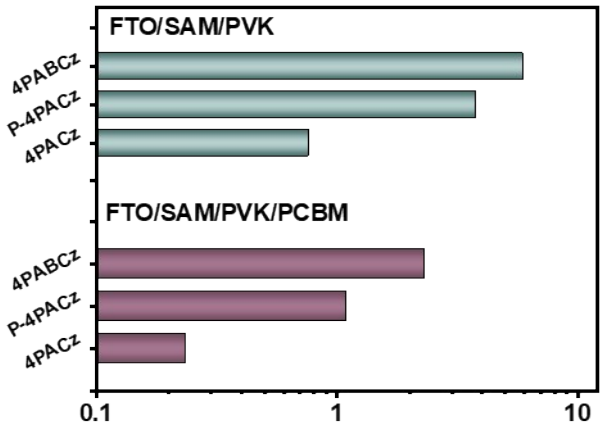

Figure S38. PLQY values of FTO/SAM/perovskite stacks and FTO/SAM/perovskite/PCBM stacks.

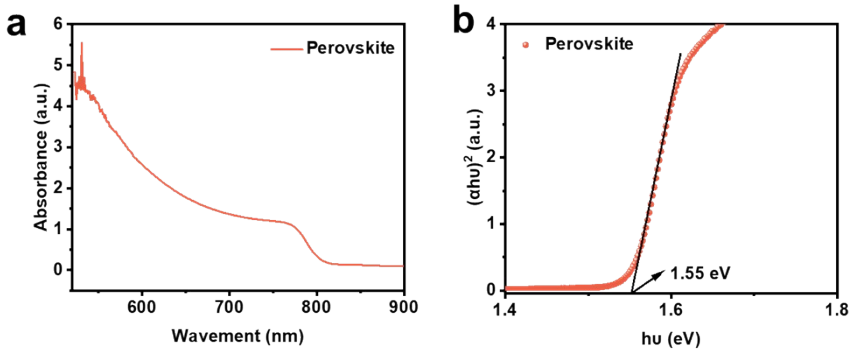

Figure S39. a) UV-vis absorption spectra and b) Tauc of perovskite films

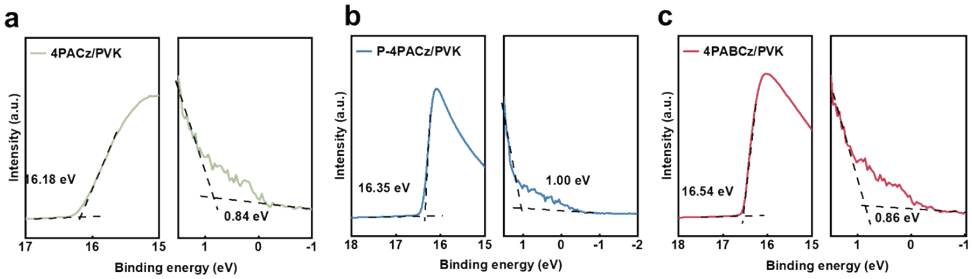

Figure S40. UPS spectra of a) perovskite deposited on 4PACz, b) perovskite deposited on P-4PACz and c) perovskite deposited on 4PABCz.

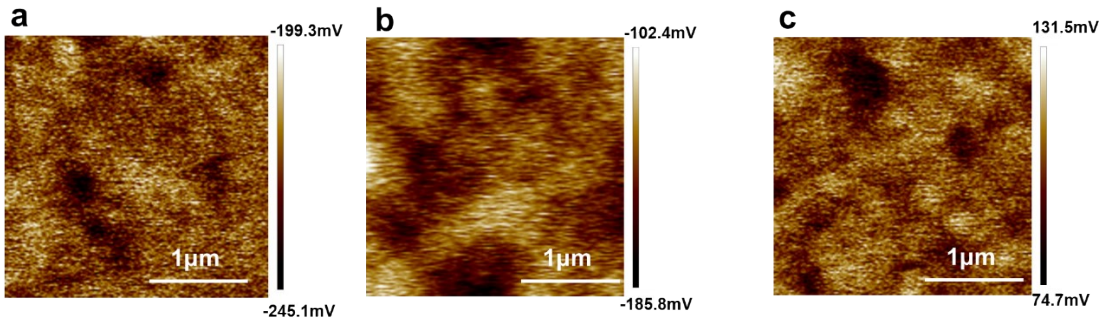

Figure S41. KPFM of perovskite films based on a) 4PACz, b) P-4PACz and c) 4PABCz films.

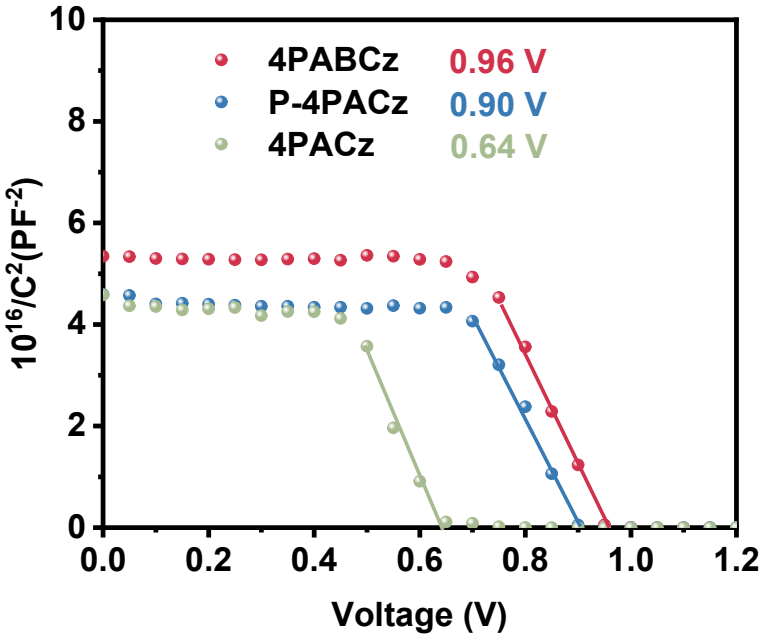

Figure S42. Mott–Schottky plots of 4PACz, P-4PACz and 4PABCz based PSCs. The curves on top of the data were extracted by linear fitting the drop region of Mott-Schottky plots, and V_{bi} was obtained via the intercept of the straight line with the x axis.

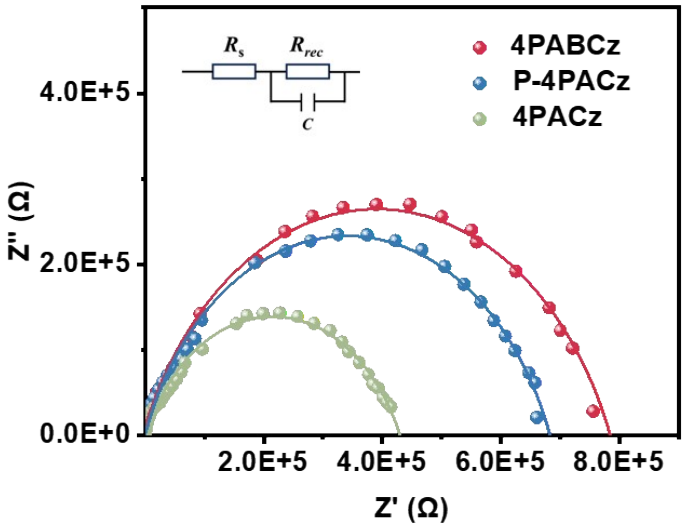

Figure S43. The fitting EIS spectra of PSCs based on 4PACz, P-4PACz and 4PABCz films.

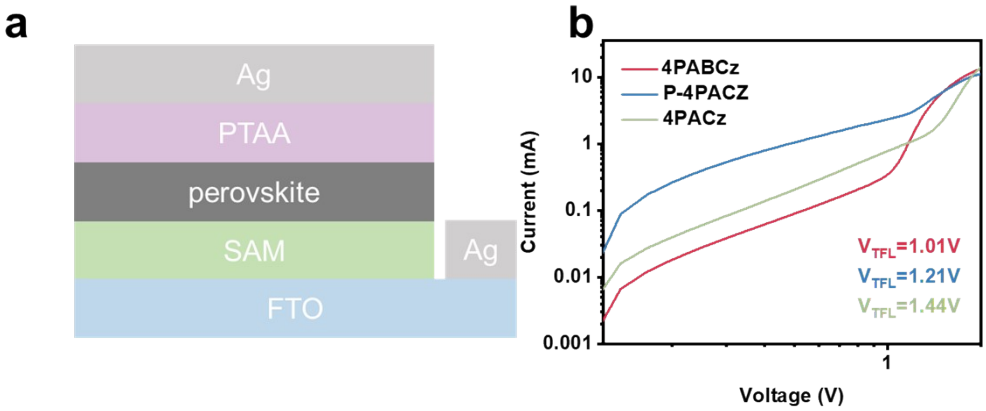

Figure S44. a) hole-only devices structure b) the space-charge-limited current (SCLC) versus voltage curves for the hole-only devices based on 4PACz, P-4PACz and 4PABCz films.

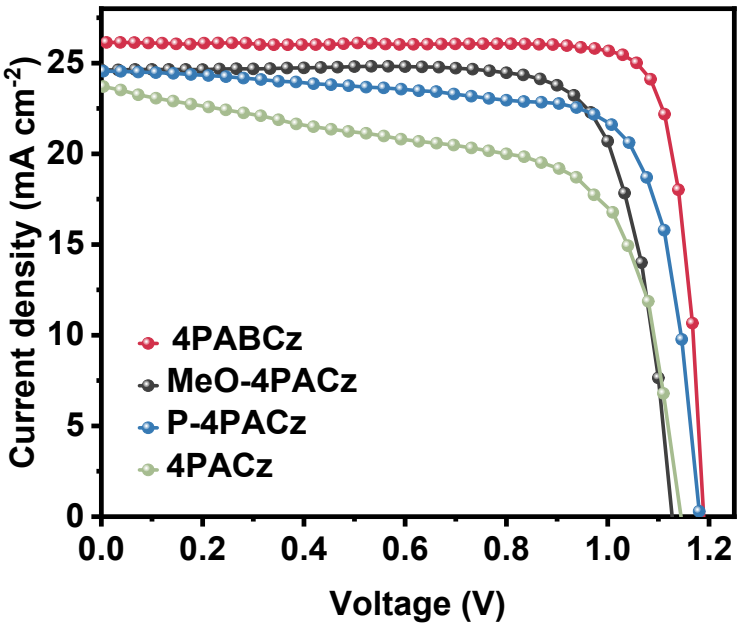

Figure S45. Champion devices with forward scan.

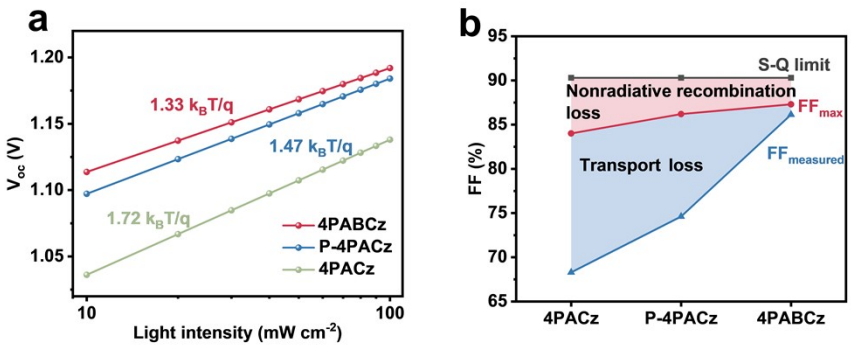

Figure S46 a) V_{OC} versus light intensity for PSCs with 4PACz, P-4PACz and 4PABCz; b) FF loss plot for 4PACz, P-4PACz and 4PABCz.

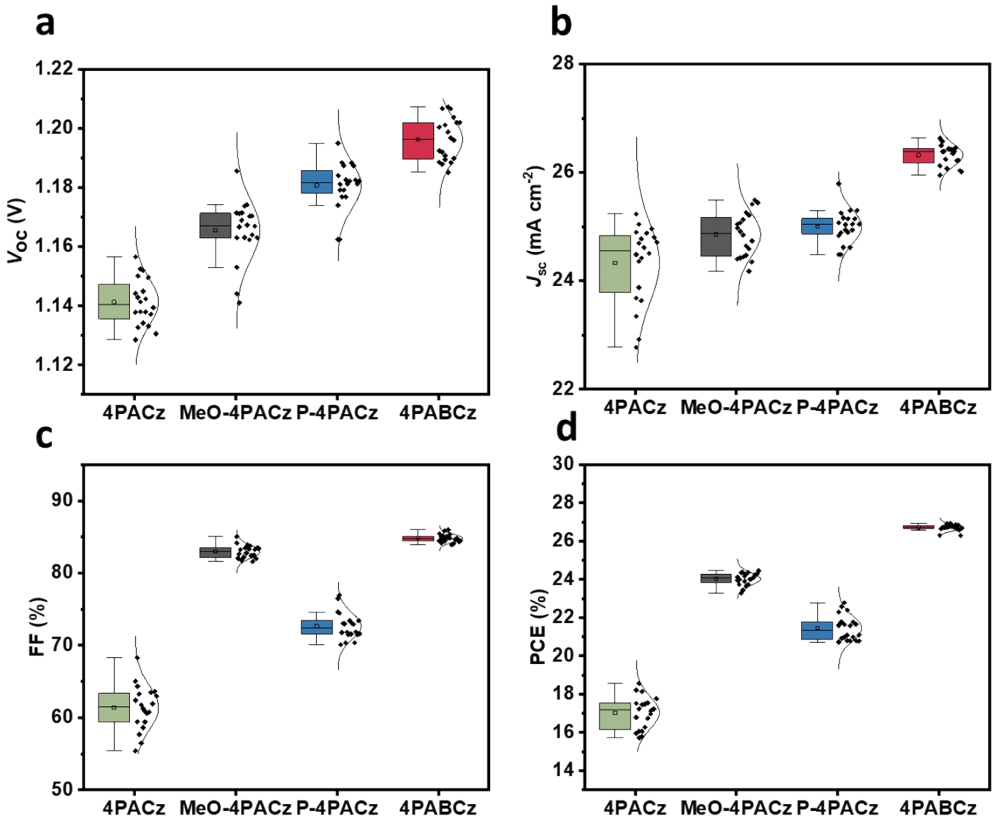

Figure S47. Statistical a) V_{OC}, b) J_{SC}, c) FF and d) PCE of the PSCs with substrates of 4PACz, P-4PACz, MeO-4PACz and 4PABCz.

福建省计量科学研究院
FUJIAN METROLOGY INSTITUTE
（国家光伏产业计量测试中心）
National PV Industry Measurement and Testing Center

检 测 报 告
Test Report

报告编号：24Q3-00625
Report No.

客户信息 Name of Custome	Shanghai Jiao Tong University and CATL
联络信息 Contact Information	800 Dongchuan Road, Minhang District, Shanghai, China
物品名称 Name of items	Inverted Perovskite Solar Cell (IV)
型号/规格 Type /Specification	Inverted PSC
物品编号 Ittems No	S21
制造厂商 Manufacturer	Chun-Chao Chen's group
物品接收日期 Items Receipt Date	2024-10-09
检测日期 Test Date	2024-10-09

批准人：黎健生 Approved by
核验员：何翔 Checked by
检测员：陈彩云 Test by

发布日期：2024 年 10 月 14 日
Date of Report Year Month Day

扫一扫 查真伪

本院/本中心地址：福州市屏东路9-3号 Address：9-3 Pingdong Road,Fuzhou,China
电话：0591-87845050 Telephone
传真：0591-87808417 Fax
邮编：350003 Post Code
网址：www.fjjl.net Web Site
咨询电话：0591-87845050 Inquire line
投诉电话：0591-87823025 Complaint Tel

未经本院/本中心书面批准，部分采用本报告内容无效。
Partly using this Report will not be admitted unless allowed by FMI/ Center.

第 1 页/共 6 页 Page of Pages

Figure S48a. The certificate of one 4PABCz inverted device (J–V characterization). The report is issued by NPVM (Chinese National PV Industry Measurement and Testing Center). The aperture area is 0.0736 cm^2 measured by NPVM.

福建省计量科学研究院
FUJIAN METROLOGY INSTITUTE
（国家光伏产业计量测试中心）
National PV Industry Measurement and Testing Center

24Q3-00625

检测结果/说明：
Results of Test and additional explanation.

1. Standard Test Condition (STC)：Total Irradiance：1000 W/m^2
Temperature：25.0 °C
Spectral Distribution：AM1.5G

2.Measurement Data and I-V/P-V Curves under STC

Forward Scan

I_{sc} (mA)	V_{oc}(V)	I_{MPP}(mA)	V_{MPP}(V)	P_{MPP} (mW)	FF(%)	A (cm^2)
1.926	1.183	1.847	1.051	1.941	85.19	0.0736

Reverse Scan

I_{sc} (mA)	V_{oc}(V)	I_{MPP}(mA)	V_{MPP}(V)	P_{MPP} (mW)	FF(%)	A (cm^2)
1.926	1.186	1.868	1.056	1.973	86.37	0.0736

Mismatch factor: 0.9907

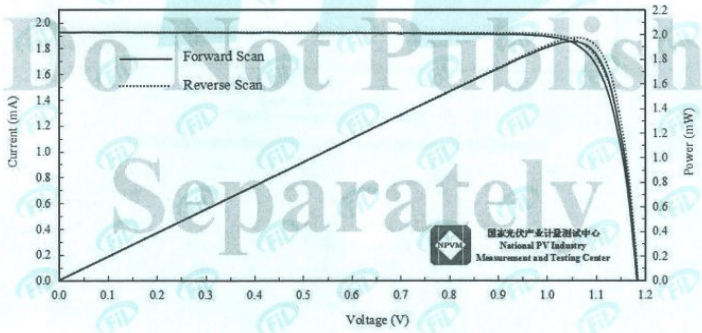

Figure 1. I-V and P-V characteristic curves of the measured sample under STC

检测报告续页专用
Continued page of test report

第 3 页/共 6 页
Page of Pages

Figure S48b. The certificate of one 4PABCz inverted device (J–V characterization). The report is issued by NPVM (Chinese National PV Industry Measurement and Testing Center). The aperture area is 0.0736 cm^2 measured by NPVM.

福建省计量科学研究院
FUJIAN METROLOGY INSTITUTE
（国家光伏产业计量测试中心）
National PV Industry Measurement and Testing Center

报告编号： 24Q3-00625
Report No.

检测结果/说明：
Results of Test and additional explanation.

3.Measurement Data and Curves for MPPT under STC

η (%)	25.96
P_{MPP} (mW)	1.911
I_{MPP} (mA)	1.810
V_{MPP} (V)	1.056

Note: Measurement data for MPPT under STC in the above table was the mean value acquired during the final 30 seconds of the 300 seconds test

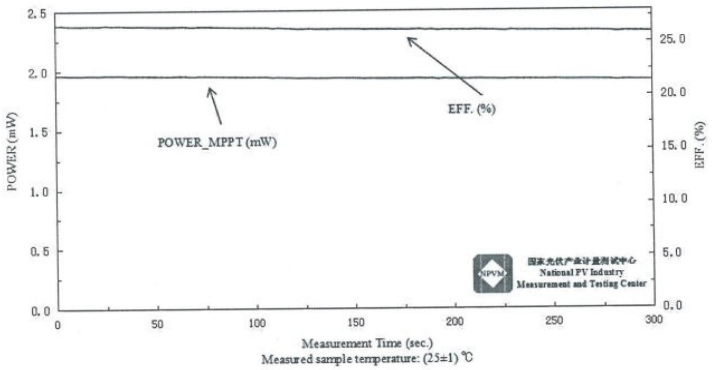

Figure 2. Measurement curves of the measured sample for MPPT

检测报告续页专用
Continued page of test report

第 4 页/共 6 页
Page of Pages

Figure S48c. The certificate of one 4PABCz inverted device (steady-state PCE characterization). The report is issued by NPVM. The stabilized PCE of 25.96% is determined from MPPT for 300 s.

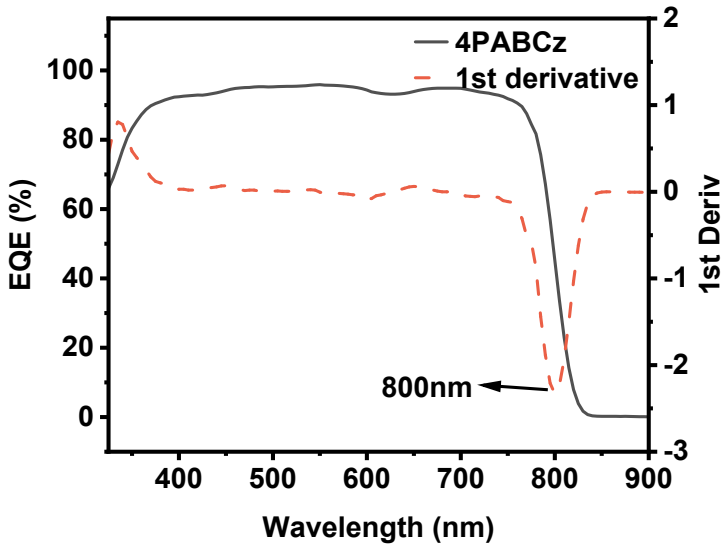

Figure S49. The corresponding EQE derivation calculation results for band gap values and derivative of perovskite films based on 4PABCz.

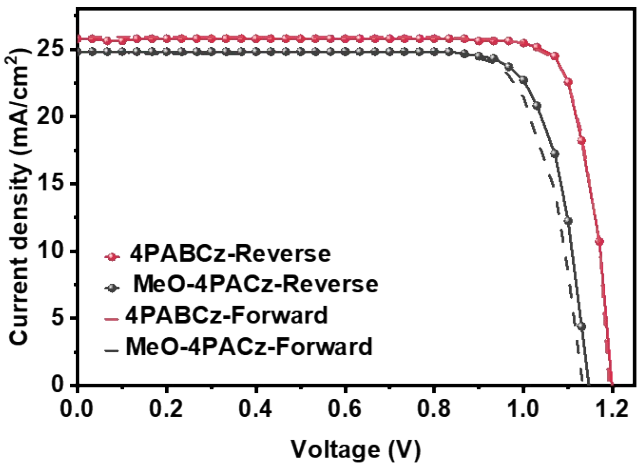

Figure S50. *J-V* curves for PSCs based on ITO with 4PABCz and MeO-4PACz.

230017163974

中国认可
国际互认
检测
TESTING
CNAS L8490

Test and Calibration Center of New Energy Device and Module,
Shanghai Institute of Microsystem and Information Technology,
Chinese Academy of Sciences (SIMIT)

Measurement Report

Report No. 23TR090802

Client Name	Shanghai Jiao Tong University
Client Address	No. 800, Dongchuan Road, Minhang District, Shanghai, China
Sample	Flexible Inverted Perovskite Solar Cell
Manufacturer	Chun-Chao Chen's Group
Measurement Date	8th September, 2023

Performed by:	Qiang Shi	**Date:** 08/09/2023
Reviewed by:	Wenjie Zhao	**Date:** 08/09/2023
Approved by:	Yucheng Liu	**Date:** 08/09/2023

Address: No.235 Chengbei Road, Jiading, Shanghai **Post Code:**201800
E-mail: solarcell@mail.sim.ac.cn **Tel:** +86-021-69976921

Figure S51a. Certified performance of flexible inverted perovskite solar cell with an area of 7.46 mm^2 based on 4PABCz at SIMIT.

====Measurement Results ====

	Forward Scan (Isc to Voc)	Reverse Scan (Voc to Isc)
Area	7.46 mm²	
Isc	1.774 mA	1.770 mA
Voc	1.181 V	1.183 V
Pmax	1.774 mW	1.790 mW
Ipm	1.713 mA	1.721 mA
Vpm	1.036 V	1.040 V
FF	84.70 %	85.47 %
Eff	23.78 %	24.00 %

- Spectral Mismatch Factor: SMM=1.0035.
- Designated illumination area defined by a thin metal mask was measured by measuring microscope.
- Test results listed in this measurement report refer exclusively to the mentioned measured sample.
- The results apply only at the time of the test, and do not imply future performance.

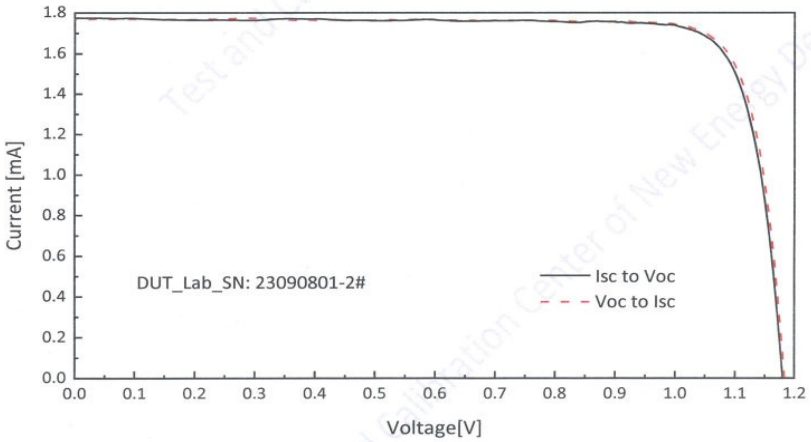

Fig.1 I-V curves of the measured sample

Figure S51b. Certified performance of flexible inverted perovskite solar cell with an area of 7.46 mm^2 based on 4PABCz at SIMIT.

Test and Calibration Center of New Energy Device and Module,
Shanghai Institute of Microsystem and Information Technology,
Chinese Academy of Sciences (SIMIT)

230017163974

中国认可
国际互认
检测
TESTING
CNAS L8490

Measurement Report

Report No. 23TR090803

Client Name	Shanghai Jiao Tong University
Client Address	No. 800, Dongchuan Road, Minhang District, Shanghai, China
Sample	Flexible Inverted Perovskite Solar Cell
Manufacturer	Chun-Chao Chen's Group
Measurement Date	8th September, 2023

Performed by:	Qiang Shi	**Date:** 08/09/2023
Reviewed by:	Wenjie Zhao	**Date:** 08/09/2023
Approved by:	Yucheng Liu	**Date:** 08/09/2023

Address: No.235 Chengbei Road, Jiading, Shanghai
Post Code:201800
E-mail: solarcell@mail.sim.ac.cn
Tel: +86-021-69976921

Figure S52a. Certified performance of flexible inverted perovskite solar cell with an area of 102.80 mm^2 based on 4PABCz at SIMIT.

====Measurement Results ====

	Forward Scan (Isc to Voc)	Reverse Scan (Voc to Isc)
Area	102.80 mm^2	
Isc	24.299 mA	24.286 mA
Voc	1.184 V	1.189 V
Pmax	23.050 mW	22.899 mW
Ipm	23.056 mA	22.940 mA
Vpm	1.000 V	0.998 V
FF	80.12 %	79.31 %
Eff	22.42 %	22.28 %

- Spectral Mismatch Factor: SMM=1.0032.
- Designated illumination area defined by a thin metal mask was measured by measuring microscope.
- Test results listed in this measurement report refer exclusively to the mentioned measured sample.
- The results apply only at the time of the test, and do not imply future performance.

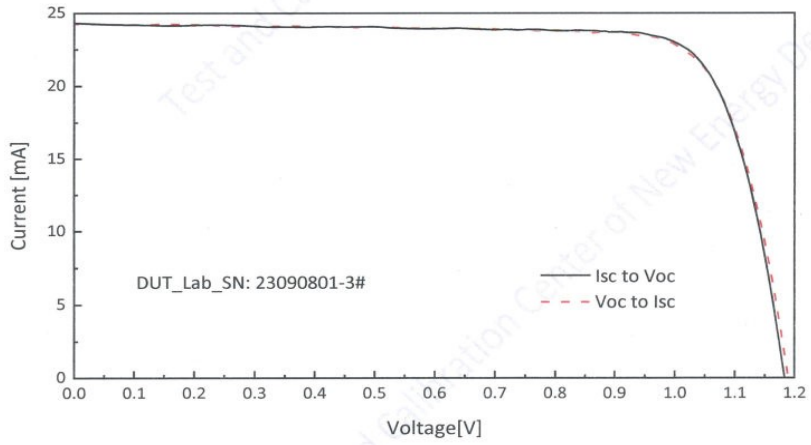

Fig.1 I-V curves of the measured sample

Figure S52b. Certified performance of flexible inverted perovskite solar cell with an area of 102.80 mm^2 based on 4PABCz at SIMIT.

Table S1. The development of inverted PSCs fabricated on ITO substrates and FTO substrates.

Year	Efficiency	Substrate structure	Reference
2018	17.8%	ITO/10% V1036 90% C4	41
	16.7%	FTO/NiMgLiO	42
2019	21.2%	ITO/MeO-2PACz/MAFA	43
	20.6%	FTO/PEDOT:PSS	44
2020	21.24%	ITO/MPA-BT-CA	45
2021	22.7%	ITO/2PACz	46
	22.44%	FTO/Br-2EPT	47
2022	25.49%	ITO/MeO-2PACz	48
	24.09%	FTO/NiOx/MeO-2PACz	49
2023	25.86%	ITO/DMAcPA	50
	25.3%	FTO/2-PACz+3-MPA	51
2024	26.69%	ITO/NiOx/Me-4PACz+NA-Me	52
	26.15%	FTO/Me-4PACz	53

Table S2. Crystal data and structural refinement for P-Cz and PB-Cz

π-scaffolds	P-Cz	PB-Cz
Empirical formula	C18 H13 N	C30 H20 N2
Formula weight	243.29	408.48
Temperature	300(2) K	293(2) K
Wavelength	1.54184 Å	1.54184 Å
Crystal system	Monoclinic	Monoclinic
Space group	P21	C2/c
a/Å	6.4624(5)	27.8850(4)
b/Å	7.3908(5)	5.60720(10) Å
c/Å	13.2977(11)	27.8067(4) Å
α/Å	90°	90°
β/Å	101.493(8)°	111.5670(10)°
γ/Å	90°	90°
Volume	622.39(8) $Å^3$	4043.37(11) $Å^3$
Z	2	8
Density (calculated)	1.298 Mg/m^3	1.342 Mg/m^3
Absorption coefficient	0.578 mm^{-1}	0.605 mm^{-1}
F(000)	256	1712
Crystal size	0.180 x 0.160 x 0.140 mm^3	0.160 x 0.140 x 0.120 mm^3
Theta range for data collection	3.392 to 76.602°.	3.409 to 77.734°.
Index ranges	-8<=h<=8, -9<=k<=6, -16<=l<=16	-34<=h<=34, -7<=k<=6, -34<=l<=34
Reflections collected	5112	26979
Independent reflections	1869 [R(int) = 0.0184]	4188 [R(int) = 0.0345]
Completeness to theta = 67.684°	99.50%	99.90%
Data/restraints/parameters	1869 / 1 / 174	4188 / 0 / 289
Goodness-of-fit on F2	1.003	1.421
Final R indices [I>2sigma(I)]	R1 = 0.0404, wR2 = 0.1050	R1 = 0.0409, wR2 = 0.1525
R indices (all data)	R1 = 0.0498, wR2 = 0.1293	R1 = 0.0446, wR2 = 0.1574
Largest diff. peak and hole	0.159 and -0.178 $e.Å^{-3}$	0.183 and -0.233 $e.Å^{-3}$

Table S3. IRI analysis.

Sample	Integration result / a.u.	Volume/ $Bohr^3$	Average interactions (=Integration result / volume) / 10^{-3} $Bohr^{-3}$
4PACz	0.184	35.656	5.17
P-4PACz	0.168	32.508	5.16
4PABCz	0.366	69.195	5.29

Table S4. Coverage factors and corresponding parameters of devices with SAMs.

	Atomic concentration (%)		
	P2p	Sn3d	P/Sn
4PACz	1.62	22.19	0.073
4PACz-washed	0.76	18.85	0.040
P-4PACz	1.2	15.38	0.078
P-4PACz-washed	1.23	24.15	0.051
4PABCz	1.42	13.8	0.103
4PABCz-washed	1.61	19.09	0.084

Table S5. The PL decay fitting parameters of SAMs/perovskite junctions and SAMs/perovskite/ PCBM.

Samples	A_1	τ_1(μs)	A_2	τ_2(μs)	τ_{ave}(μs)
4PACZ	156.746	0.100	88.410	1.042	0.905
P-4PACz	210.329	1.011	53.497	4.191	2.643
4PABCz	219.635	0.868	53.488	5.049	3.319

Table S6. PLQY and QFLS values of FTO/SAM/perovskite stacks, FTO/SAM/perovskite/PCBM stacks, and FTO/SAM/perovskite/PDI/PCBM stacks.

Samples	PLQY	QFLS
4PACz/perovskite	0.76	1.152
	0.68	1.149
P-4PACz/perovskite	3.77	1.192
	3.83	1.193
4PABCz/perovskite	5.89	1.203
	5.44	1.201
4PACz/perovskite/PDI/PCBM	0.53	1.142
	0.50	1.141
P-4PACz/perovskite/PDI/PCBM	3.24	1.188
	2.86	1.185
4PABCz/perovskite/PDI/PCBM	4.01	1.193
	4.39	1.196
4PACz/perovskite/PCBM	0.24	1.121
	0.25	1.122
P-4PACz/perovskite/PCBM	1.09	1.160
	1.12	1.161
4PABCz/perovskite/PCBM	2.30	1.179
	2.49	1.181

Table S7. Non-radiative recombination loss.

Samples	Bandgap (eV)	QFLS $_{rad}$ (eV)	$q\Delta V_{oc-imp}^{nonrad}$ (V)
4PACz	1.55	1.277	0.125
P-4PACz	1.55	1.276	0.084
4PABCz	1.55	1.276	0.076

Table S8. Photovoltaic parameters (scanned forward) of champion devices treated by 4PACz, P-4PACz, MeO-4PACz, 4PABCz based on FTO

Samples	V_{oc} (V)	J_{sc} (mA/cm^2)	FF (%)	PCE (%)
4PACz	1.14	23.68	65.04	17.53
P-4PACz	1.18	24.58	75.20	21.77
MeO-4PACz	1.15	25.66	81.13	23.94
4PABCz	1.19	26.12	85.11	26.44

Table S9. Efficiency of recently reported inverted PSCs based on FTO.

Reference	E_g (eV)	V_{oc} (V)	J_{sc} (mA cm^{-2})	FF (%)	PCE (%)	Certified PCE (%)
Nature, **2023**, *624*, 289–294.[51]	1.54	1.16	25.8	84.1	25.3	24.8 (QSS)
*Science,***2023***, 382*, 810-815.[54]	\	1.17	26.2	85.8	26.4	25.1 (QSS)
Angew. Chem. Int. Ed. **2024**, *63*, e202409689.[55]	\	1.17	24.83	86.24	25.05	\
*Science,***2024***, 384*, 878-884.[56]	1.53	1.18	25.9	85.4	26	\
*Science,***2023***, 382*, 1399-1404.[57]	1.52	1.16	26.15	84.1	25.5	25.2 (QSS)
Energy Environ. Sci., **2024**,*17*, 1153-1162.[53]	1.55	1.18	25.67	86.47	26.15	25.52 (QSS)
Adv. Mater. **2024**, *36*, 2404797.[58]	1.54	1.19	25.46	85.09	25.78	25.36
Adv. Energy Mater. **2024**, *14*, 2304486.[59]	1.52	1.17	25.77	84.02	25.35	24.87
Adv. Energy Mater. **2024**, *14*, 2303941.[1]	1.55	1.21	25.18	84.23	25.6	24.48
Energy Environ. Sci., **2024**, *17*, 7342-7354.[60]	1.53	1.169	26.07	85.06	25.92	25.77
Adv. Mater. **2024**, *36*, 2401537.[61]	\	1.16	25.59	84.74	25.15	\
This work	1.55	1.192	26.20	86.14	26.90	26.81 (MPP:25.96%)

QSS is quasi-steady-state, MPP is maximum-power-point tracking.

Table S10. Photovoltaic parameters of champion devices treated by MeO-4PACz and 4PABCz on ITO.

Samples	Scan direction	V_{oc} (V)	J_{sc}(mA cm^{-2})	FF (%)	PCE (%)
MeO-4PACz	Forward	1.35	24.78	79.51	22.36
	Reverse	1.15	24.85	80.67	22.99
4PABCz	Forward	1.19	25.97	83.88	25.93
	Reverse	1.20	25.75	84.54	26.08

Reference

1 A. Sun, C. Tian, R. Zhuang, C. Chen, Y. Zheng, X. Wu, C. Tang, Y. Liu, Z. Li, B. Ouyang, J. Du, Z. Li, J. Cai, J. Chen, X. Wu, Y. Hua and C.-C. Chen, *Adv. Energy Mater.*, 2024, **14**, 2303941.

2 P. J. Stephens, F. J. Devlin, C. F. Chabalowski and M. J. Frisch, *J. Phys. Chem.*, 1994, **98**, 11623–11627.

3 R. Krishnan, J. S. Binkley, R. Seeger and J. A. Pople, *J. Chem. Phys.*, 1980, **72**, 650–654.

4 A. D. McLean and G. S. Chandler, *J. Chem. Phys.*, 1980, **72**, 5639–5648.

5 A. Schäfer, C. Huber and R. Ahlrichs, *J. Chem. Phys.*, 1994, **100**, 5829–5835.

6 F. Weigend and R. Ahlrichs, *Phys. Chem. Chem. Phys.*, 2005, **7**, 3297–3305.

7 Gaussian 09, Revision A.02, M. J. Frisch, G. W. Trucks, H. B. Schlegel, G. E. Scuseria, M. A. Robb, J. R. Cheeseman, G. Scalmani, V. Barone, G. A. Petersson, H. Nakatsuji, X. Li, M. Caricato, A. Marenich, J. Bloino, B. G. Janesko, R. Gomperts, B. Mennucci, H. P. Hratchian, J. V. Ortiz, A. F. Izmaylov, J. L. Sonnenberg, D. Williams-Young, F. Ding, F. Lipparini, F. Egidi, J. Goings, B. Peng, A. Petrone, T. Henderson, D. Ranasinghe, V. G. Zakrzewski, J. Gao, N. Rega, G. Zheng, W. Liang, M. Hada, M. Ehara, K. Toyota, R. Fukuda, J. Hasegawa, M. Ishida, T. Nakajima, Y. Honda, O. Kitao, H. Nakai, T. Vreven, K. Throssell, J. A. Montgomery, Jr., J. E. Peralta, F. Ogliaro, M. Bearpark, J. J. Heyd, E. Brothers, K. N. Kudin, V. N. Staroverov, T. Keith, R. Kobayashi, J. Normand, K. Raghavachari, A. Rendell, J. C. Burant, S. S. Iyengar, J. Tomasi, M. Cossi, J. M. Millam, M. Klene, C. Adamo, R. Cammi, J. W. Ochterski, R. L. Martin, K. Morokuma, O. Farkas, J. B. Foresman, and D. J. Fox, Gaussian, Inc., Wallingford CT, 2016.

8 C. Lee, W. Yang and R. G. Parr, *Phys. Rev. B*, 1988, **37**, 785–789.

9 W. Humphrey, A. Dalke and K. Schulten, *J. Mol. Graph.*, 1996, **14**, 33–38.

10 T. Lu, *J. Chem. Phys.*, 2024, **161**, 082503.

11 J. Zhang and T. Lu, *Phys. Chem. Chem. Phys. PCCP*, 2021, **23**, 20323–20328.

12 S. Grimme, J. Antony, S. Ehrlich and H. Krieg, *J. Chem. Phys.*, 2010, **132**, 154104.

13 P. J. Hay and W. R. Wadt, *J. Chem. Phys.*, 1985, **82**, 299–310.

14 T. Lu and Q. Chen, *Chemistry–Methods*, 2021, **1**, 231–239.

15 Z. Liu, T. Lu and Q. Chen, *Carbon*, 2021, **171**, 514–523.

16 G. Kresse and D. Joubert, *Phys. Rev. B*, 1999, **59**, 1758–1775.

17 G. Kresse and J. Furthmüller, *Phys. Rev. B*, 1996, **54**, 11169–11186.

18 J. P. Perdew, K. Burke and M. Ernzerhof, *Phys. Rev. Lett.*, 1996, **77**, 3865–3868.

19 P. E. Blöchl, *Phys. Rev. B*, 1994, **50**, 17953–17979.

20 K. Momma and F. Izumi, *J. Appl. Crystallogr.*, 2011, **44**, 1272–1276.

21 T. D. Kühne, M. Iannuzzi, M. Del Ben, V. V. Rybkin, P. Seewald, F. Stein, T. Laino, R. Z. Khaliullin, O. Schütt, F. Schiffmann, D. Golze, J. Wilhelm, S. Chulkov, M. H. Bani-Hashemian, V. Weber, U. Borštnik, M. Taillefumier, A. S. Jakobovits, A. Lazzaro, H. Pabst, T. Müller, R. Schade, M. Guidon, S. Andermatt, N. Holmberg, G. K. Schenter, A. Hehn, A. Bussy, F. Belleflamme, G. Tabacchi, A. Glöß, M. Lass, I. Bethune, C. J. Mundy, C. Plessl, M. Watkins, J. VandeVondele, M. Krack and J.

Hutter, *J. Chem. Phys.*, 2020, **152**, 194103.
22 M. J. van Setten, M. Giantomassi, E. Bousquet, M. J. Verstraete, D. R. Hamann, X. Gonze and G.-M. Rignanese, *Comput. Phys. Commun.*, 2018, **226**, 39–54.
23 L. Bengtsson, *Phys. Rev. B*, 1999, **59**, 12301–12304.
24 J. VandeVondele and J. Hutter, *J. Chem. Phys.*, 2007, **127**, 114105.
25 S. Nosé, *Mol. Phys.*, 1984, **52**, 255–268.
26 S. Nosé, *J. Chem. Phys.*, 1984, **81**, 511–519.
27 A. Stukowski and K. Albe, *Model. Simul. Mater. Sci. Eng.*, 2010, **18**, 085001.
28 A. P. Thompson, H. M. Aktulga, R. Berger, D. S. Bolintineanu, W. M. Brown, P. S. Crozier, P. J. in 't Veld, A. Kohlmeyer, S. G. Moore, T. D. Nguyen, R. Shan, M. J. Stevens, J. Tranchida, C. Trott and S. J. Plimpton, *Comput. Phys. Commun.*, 2022, **271**, 108171.
29 L. Verlet, *Phys. Rev.*, 1967, **159**, 98–103.
30 W. G. Hoover, *Phys. Rev. A*, 1985, **31**, 1695–1697.
31 A. V. Bandura, J. O. Sofo and J. D. Kubicki, *J. Phys. Chem. B*, 2006, **110**, 8386–8397.
32 J. Wang, R. M. Wolf, J. W. Caldwell, P. A. Kollman and D. A. Case, *J. Comput. Chem.*, 2004, **25**, 1157–1174.
33 P. Caprioglio, M. Stolterfoht, C. M. Wolff, T. Unold, B. Rech, S. Albrecht and D. Neher, *Adv. Energy Mater.*, 2019, **9**, 1901631.
34 P. Caprioglio, J. A. Smith, R. D. J. Oliver, A. Dasgupta, S. Choudhary, M. D. Farrar, A. J. Ramadan, Y.-H. Lin, M. G. Christoforo, J. M. Ball, J. Diekmann, J. Thiesbrummel, K.-A. Zaininger, X. Shen, M. B. Johnston, D. Neher, M. Stolterfoht and H. J. Snaith, *Nat. Commun.*, 2023, **14**, 932.
35 F. Li, X. Deng, F. Qi, Z. Li, D. Liu, D. Shen, M. Qin, S. Wu, F. Lin, S.-H. Jang, J. Zhang, X. Lu, D. Lei, C.-S. Lee, Z. Zhu and A. K.-Y. Jen, *J. Am. Chem. Soc.*, 2020, **142**, 20134–20142.
36 W. Zhao, J. Ding, Y. Zou, C. Di and D. Zhu, *Chem. Soc. Rev.*, 2020, **49**, 7210–7228.
37 R. H. Bube, *J. Appl. Phys.*, 1962, **33**, 1733–1737.
38 Y. Luo, J. Zhu, X. Yin, W. Jiao, Z. Gao, Y. Xu, C. Wang, Y. Wang, H. Lai, H. Huang, J. Luo, J. Wang, J. You, Z. Zhang, X. Hao, G. Zeng, S. Ren, Z. Li, F. Fu, M. Li, C. Xiao, C. Chen and D. Zhao, *Adv. Energy Mater.*, 2024, **14**, 2304429.
39 C. Zhang, Y. Son, H. Kim, S.-H. Lee, X. Liang, G. Fu, S.-U. Lee, D.-A. Park, Q. Jiang, K. Zhu and N.-G. Park, *Joule*, 2024, **8**, 1394–1411.
40 Y. Liu, C. Tang, A. Sun, R. Zhuang, Y. Zheng, C. Tian, X. Wu, Z. Li, B. Ouyang, J. Du, Z. Li, Y. Hua and C.-C. Chen, *Mater. Horiz.*, 2023, **10**, 5763–5774.
41 A. Magomedov, A. Al-Ashouri, E. Kasparavičius, S. Strazdaite, G. Niaura, M. Jošt, T. Malinauskas, S. Albrecht and V. Getautis, *Adv. Energy Mater.*, 2018, **8**, 1801892.
42 R. Fang, S. Wu, W. Chen, Z. Liu, S. Zhang, R. Chen, Y. Yue, L. Deng, Y.-B. Cheng, L. Han and W. Chen, *ACS Nano*, 2018, **12**, 2403–2414.
43 A. Al-Ashouri, A. Magomedov, M. Roß, M. Jošt, M. Talaikis, G. Chistiakova, T. Bertram, J. A. Márquez, E. Köhnen, E. Kasparavičius, S. Levcenco, L. Gil-Escrig, C. J. Hages, R. Schlatmann, B. Rech, T. Malinauskas, T. Unold, C. A. Kaufmann,

L. Korte, G. Niaura, V. Getautis and S. Albrecht, *Energy Environ. Sci.*, 2019, **12**, 3356–3369.
44 D. Yang, X. Zhang, K. Wang, C. Wu, R. Yang, Y. Hou, Y. Jiang, S. Liu and S. Priya, *Nano Lett.*, 2019, **19**, 3313–3320.
45 Y. Wang, Q. Liao, J. Chen, W. Huang, X. Zhuang, Y. Tang, B. Li, X. Yao, X. Feng, X. Zhang, M. Su, Z. He, T. J. Marks, A. Facchetti and X. Guo, *J. Am. Chem. Soc.*, 2020, **142**, 16632–16643.
46 S. Gharibzadeh, P. Fassl, I. M. Hossain, P. Rohrbeck, M. Frericks, M. Schmidt, T. Duong, M. R. Khan, T. Abzieher, B. A. Nejand, F. Schackmar, O. Almora, T. Feeney, R. Singh, D. Fuchs, U. Lemmer, J. P. Hofmann, S. A. L. Weber and U. W. Paetzold, *Energy Environ. Sci.*, 2021, **14**, 5875–5893.
47 A. Ullah, K. H. Park, H. D. Nguyen, Y. Siddique, S. F. A. Shah, H. Tran, S. Park, S. I. Lee, K. Lee, C. Han, K. Kim, S. Ahn, I. Jeong, Y. S. Park and S. Hong, *Adv. Energy Mater.*, 2022, **12**, 2103175.
48 Q. Jiang, J. Tong, Y. Xian, R. A. Kerner, S. P. Dunfield, C. Xiao, R. A. Scheidt, D. Kuciauskas, X. Wang, M. P. Hautzinger, R. Tirawat, M. C. Beard, D. P. Fenning, J. J. Berry, B. W. Larson, Y. Yan and K. Zhu, *Nature*, 2022, **611**, 278–283.
49 Y. Zhang, C. Li, E. Bi, T. Wang, P. Zhang, X. Yang and H. Chen, *Adv. Energy Mater.*, 2022, **12**, 2202191.
50 Q. Tan, Z. Li, G. Luo, X. Zhang, B. Che, G. Chen, H. Gao, D. He, G. Ma, J. Wang, J. Xiu, H. Yi, T. Chen and Z. He, *Nature*, 2023, **620**, 545–551.
51 S. M. Park, M. Wei, N. Lempesis, W. Yu, T. Hossain, L. Agosta, V. Carnevali, H. R. Atapattu, P. Serles, F. T. Eickemeyer, H. Shin, M. Vafaie, D. Choi, K. Darabi, E. D. Jung, Y. Yang, D. B. Kim, S. M. Zakeeruddin, B. Chen, A. Amassian, T. Filleter, M. G. Kanatzidis, K. R. Graham, L. Xiao, U. Rothlisberger, M. Grätzel and E. H. Sargent, *Nature*, 2023, **624**, 289–294.
52 S. Liu, J. Li, W. Xiao, R. Chen, Z. Sun, Y. Zhang, X. Lei, S. Hu, M. Kober-Czerny, J. Wang, F. Ren, Q. Zhou, H. Raza, Y. Gao, Y. Ji, S. Li, H. Li, L. Qiu, W. Huang, Y. Zhao, B. Xu, Z. Liu, H. J. Snaith, N.-G. Park and W. Chen, *Nature*, 2024, **632**, 536–542.
53 Y. Zheng, Y. Li, R. Zhuang, X. Wu, C. Tian, A. Sun, C. Chen, Y. Guo, Y. Hua, K. Meng, K. Wu and C.-C. Chen, *Energy Environ. Sci.*, 2024, **17**, 1153–1162.
54 C. Liu, Y. Yang, H. Chen, J. Xu, A. Liu, A. S. R. Bati, H. Zhu, L. Grater, S. S. Hadke, C. Huang, V. K. Sangwan, T. Cai, D. Shin, L. X. Chen, M. C. Hersam, C. A. Mirkin, B. Chen, M. G. Kanatzidis and E. H. Sargent, *Science*, 2023, **382**, 810–815.
55 Y. Yang, R. Chen, J. Wu, Z. Dai, C. Luo, Z. Fang, S. Wan, L. Chao, Z. Liu and H. Wang, *Angew. Chem. Int. Ed.*, 2024, **63**, e202409689.
56 T. Duan, S. You, M. Chen, W. Yu, Y. Li, P. Guo, J. J. Berry, J. M. Luther, K. Zhu and Y. Zhou, *Science*, 2024, **384**, 878–884.
57 S. Yu, Z. Xiong, H. Zhou, Q. Zhang, Z. Wang, F. Ma, Z. Qu, Y. Zhao, X. Chu, X. Zhang and J. You, *Science*, 2023, **382**, 1399–1404.
58 C. Tian, A. Sun, R. Zhuang, Y. Zheng, X. Wu, B. Ouyang, J. Du, Z. Li, X. Wu, J. Chen, J. Cai, Y. Hua and C.-C. Chen, *Adv. Mater.*, 2024, **36**, 2404797.
59 Y. Zheng, C. Tian, X. Wu, A. Sun, R. Zhuang, C. Tang, Y. Liu, Z. Li, B. Ouyang, J.

Du, Z. Li, X. Wu, J. Chen, J. Cai and C.-C. Chen, *Adv. Energy Mater.*, 2024, **14**, 2304486.
60 X. Chen, Q. Wang, H. Wei, J. Yang, Y. Yao, W. Tang, W. Qiu, X. Xu, L. Song, Y. Wu and Q. Peng, *Energy Environ. Sci.*, 2024, **17**, 7342–7354.
61 J. Wu, P. Yan, D. Yang, H. Guan, S. Yang, X. Cao, X. Liao, P. Ding, H. Sun and Z. Ge, *Adv. Mater.*, 2024, **36**, 2401537.